

# Impact of grids and dynamical cores in CESM2.2 on the surface mass balance of the Greenland Ice Sheet

Adam R. Herrington<sup>1</sup>, Peter H. Lauritzen<sup>1</sup>, Marcus Lofverstrom<sup>2</sup>, William H. Lipscomb<sup>1</sup>, Andrew Gettelman<sup>1</sup> and Mark A. Taylor<sup>3</sup>

<sup>1</sup>National Center for Atmospheric Research, 1850 Table Mesa Drive, Boulder, Colorado, USA

<sup>2</sup>Department of Geosciences, University of Arizona, 1040 E. 4th Street, Tucson, Arizona USA

<sup>3</sup>Sandia National Laboratories, Albuquerque, New Mexico, USA

## Key Points:

- The CESM2.2 release includes several enhancements to the spectral-element dynamical core, including two Arctic refined mesh configurations.
- Quasi-uniform unstructured** grids degrade the Greenland Ice Sheet mass balance compared to latitude-longitude grids, **at the conventional 1° resolution**.
- The refined Arctic meshes substantially improve the surface mass balance over **conventional grid resolutions**.

15      **Abstract**

16      Six different configurations, a mixture of grids and atmospheric dynamical cores  
 17      available in the Community Earth System Model, version 2.2 (CESM2.2), are evaluated  
 18      for their skill in representing the climate of the Arctic and the surface mass balance of  
 19      the Greenland Ice Sheet (GrIS). The finite-volume dynamical core uses structured, latitude-  
 20      longitude grids, whereas the spectral-element dynamical core is built with unstructured  
 21      meshes, allowing for flexible grid structures such as quasi-uniform grid spacing globally.  
 22      The  $1^{\circ}$ – $2^{\circ}$  latitude-longitude and quasi-uniform unstructured grids systematically over-  
 23      estimate both accumulation and ablation over the GrIS. Of these  $1^{\circ}$ – $2^{\circ}$  grids, the latitude-  
 24      longitude grids outperform the quasi-uniform unstructured grids because they have more  
 25      degrees of freedom to represent the GrIS. Two Arctic-refined meshes, with  $1/4^{\circ}$  and  $1/8^{\circ}$   
 26      refinement over Greenland, were developed for the spectral-element dynamical core and  
 27      are documented here as newly supported configurations in CESM2.2. The Arctic meshes  
 28      substantially improve the simulated clouds and precipitation rates in the Arctic. Over  
 29      Greenland, these meshes skillfully represent accumulation and ablation processes, lead-  
 30      ing to a more realistic GrIS surface mass balance. As CESM is in the process of tran-  
 31      sitioning away from conventional latitude-longitude grids, these new Arctic-refined meshes  
 32      improve the representation of polar processes in CESM by recovering resolution lost in  
 33      the transition to quasi-uniform grids, albeit at increased computational cost.

34      **Plain Language Summary**

35      The mass balance of Earth's big ice sheets is crucially important for understand-  
 36      ing controls on global sea-level rise. However, the scale of the processes needed to rep-  
 37      resent ice sheet mass balance is challenging to resolve in conventional Earth System Mod-  
 38      els. This study evaluates the ability of different grids and atmospheric solvers (i.e., the  
 39      dynamical core) in CESM2.2 to resolve the surface mass balance (SMB) of the Green-  
 40      land Ice Sheet. We show that the ongoing transition away from latitude-longitude grids,  
 41      towards quasi-uniform unstructured grids in CESM2.2 leads to a degradation of the sim-  
 42      ultated SMB. Two variable-resolution grids with enhanced resolution over Greenland are  
 43      developed and incorporated into the release of CESM2.2, which substantially improves  
 44      the SMB over the latitude longitude grids.

45      **1 Introduction**

46      General Circulation Models (GCMs) are powerful tools for understanding the me-  
 47      teorology and climate of the high latitudes, which are among the most sensitive regions  
 48      on Earth to global and environmental change. GCMs differ vastly in their numerical treat-  
 49      ment of polar regions because of the so-called *pole problem* (Williamson, 2007). The pole  
 50      problem refers to numerical instability arising from the convergence of meridian lines into  
 51      polar singularities on latitude-longitude grids (e.g., Figure 1a, hereafter referred to as  
 52      *lat-lon* grids). Depending on the numerics, methods exist to suppress this instability, and  
 53      lat-lon grids may be advantageous for polar processes by representing structures with  
 54      finer resolution than elsewhere in the computational domain. With the recent trend to-  
 55      wards quasi-uniform unstructured grids, any potential benefits of lat-lon grids in polar  
 56      regions may be lost (hereafter, *quasi-uniform* refers to approximately isotropic grids, in  
 57      contrast to lat-lon grids, which are highly anisotropic due to the polar singularity). In  
 58      this study, we evaluate a number of grids and dynamical cores (hereafter referred to as  
 59      *dycores*) available in the Community Earth System Model, version 2.2 (CESM2.2; Dan-  
 60      abasoglu et al., 2020), including new variable-resolution grids (i.e., grids with enhanced  
 61      resolution over a particular region), to understand their impacts on the simulated Arctic  
 62      climate. We focus specifically on the climate and surface mass balance of the Green-  
 63      land Ice Sheet.

In the 1970s, the pole problem was largely defeated through the adoption of efficient spectral transform methods in GCMs (see Williamson, 2007, and references therein). These methods transform grid point fields into a global, isotropic representation in wave space, where linear operators (e.g., horizontal derivatives) in the (truncated) equation set can be solved exactly. While spectral transform methods are still used today, local numerical methods have become desirable for their ability to run efficiently on massively parallel systems. The pole problem has thus re-emerged in contemporary climate models that use lat-lon grids, and some combination of reduced grids (modified lat-lon grids, with cells near the polar singularity elongated in the zonal direction) and polar filters are necessary to ameliorate this numerical instability (Jablonowski & Williamson, 2011). Polar filters subdue the growth of unstable computational modes by applying additional damping to the numerical solution over polar regions. This damping reduces the effective resolution in polar regions such that the resolved scales are *approximately* the same everywhere on the grid. We emphasize *approximately*, since it is conceivable that marginal increases in effective resolution occur over polar regions in lat-lon grids, despite polar filtering, since resolved waves can be represented with more grid points than at lower latitudes.

Dycores built on lat-lon grids have some advantages over [dycores built on](#) unstructured grids. Lat-lon coordinate lines are orthogonal, and aligned with zonally symmetric circulations that characterize many large-scale features of Earth's atmosphere. Lauritzen et al. (2010) has experimented with rotating lat-lon models such that their coordinate lines no longer align with an idealized, zonally balanced circulation. For the finite-volume lat-lon dycore considered in this paper (hereafter *FV*), numerical errors were shown to be largest when the polar singularity is rotated into the baroclinic zone (45°N latitude), generating spurious wave growth much earlier in the simulation than for other rotation angles. This illustrates the advantages of coordinate surfaces aligned with latitude bands, albeit an extreme example where the polar singularity and the polar filter are also contributing to the spurious wave growth. The unstructured grids all generate spurious baroclinic waves earlier in the simulations than the (unrotated) lat-lon models, although the unstructured model considered in this paper, the spectral-element dycore (hereafter *SE*), holds a balanced zonal flow without spurious wave growth appreciably longer than the rotated FV experiments (Lauritzen et al., 2010). And unlike FV, the SE dycore has the same error characteristics regardless of how the grid is rotated.

The polar filter in the FV model impedes efficiency at large processor (CPU) counts because it requires a spectral transform, which [has a](#) large communication overhead (Suarez & Takacs, 1995; Dennis et al., 2012). Unstructured grids support quasi-uniform grid spacing globally, and there is no pole problem (e.g., Figure 1c). [This is in part why](#) unstructured grids are becoming more common; their improved performance on massively parallel systems and lack of constraints on grid structure (Taylor et al., 1997; Putman & Lin, 2007; Wan et al., 2013). This increased grid flexibility allows for the adoption of variable-resolution grids (e.g., Figure 2; hereafter abbreviated as *VR*), sometimes referred to as regional grid refinement. In principle, grid refinement over polar regions can make up for any loss of resolution in transitioning away from lat-lon grids (e.g., Figure 2). However, local grid refinement comes at the cost of a smaller CFL-limited time step in the refined region; the CFL-condition — short for Courant–Friedrichs–Lowy condition — is a necessary condition for numerical stability when using discrete data in time and space.

We emphasize that the pole problem is a distinctive feature of the dycore in atmospheric models. Polar filters do not directly interfere with the physical parameterizations, nor do they have any bearing on the surface models; e.g., the land model can take full advantage of the greater number of grid cells in polar regions on lat-lon grids. This is particularly relevant for the surface mass balance ([SMB; the integrated sum of precipitation and runoff](#)) of the Greenland Ice Sheet, which relies on hydrological processes represented in the land model.

The SMB of the Greenland Ice Sheet (hereafter *GrIS*) is determined by processes occurring over a range of scales that are difficult to represent in GCMs (Pollard, 2010). GrIS precipitation is concentrated at the ice-sheet margins, where steep topographic slopes drive orographic precipitation. The truncated topography used by low resolution GCMs enables moisture to penetrate well into the GrIS interior, manifesting as a positive precipitation bias (Pollard & Groups, 2000; Van Kampenhout et al., 2019). GrIS ablation areas ([marginal regions where the annual SMB is negative](#)) are typically less than 100 km wide and are confined to low-lying areas or regions with low precipitation. These narrow ablation zones are not fully resolved in low-resolution GCMs, and may further degrade the simulated SMB. For example, CESM, version 2.0 (CESM2) underestimates ablation in the northern GrIS, leading to unrealistic ice advance when run with an interactive ice sheet component (Lofverstrom et al., 2020).

Regional climate models (RCMs) are commonly relied upon to provide more accurate SMB estimates. The limited area domain used by RCMs permits the use of high-resolution grids capable of resolving SMB processes, and can skillfully simulate the GrIS SMB (Box et al., 2004; Rae et al., 2012; Van Angelen et al., 2012; Fettweis et al., 2013; Mottram et al., 2017; Noël et al., 2018). However, unlike GCMs, RCMs are not a freely evolving system, and the atmospheric state must be prescribed at the lateral boundaries of the model domain. The inability of the RCM solution to influence larger-scale dynamics outside the RCM domain (due to the prescribed boundary conditions) severely limits this approach from properly representing the role of the GrIS in the climate system. In addition, the boundary conditions are derived from a separate host model, which introduces inconsistencies due to differences in model design between the host model and the RCM.

In order to retain the benefits of RCMs in a GCM, Van Kampenhout et al. (2019) used the VR capabilities of the SE dycore in CESM, generating [grids](#) where Greenland is represented with [up to](#)  $1/4^\circ$  resolution, and elsewhere with the more conventional  $1^\circ$  resolution. The simulated SMB compared favorably to the SMB from RCMs and observations. The VR approach is therefore emerging as a powerful tool for simulating and understanding the GrIS and its response to different forcing scenarios.

The SE dycore has been included in the model since CESM version 1, but has been under active development ever since. This includes the switch to a dry-mass vertical coordinate (Lauritzen et al., 2018) and incorporation of an accelerated multi-tracer transport scheme (Lauritzen et al., 2017), made available in CESM2. This paper documents several additional enhancements to the SE dycore as part of the release of CESM2.2. These include three new VR configurations (Figure 2), two Arctic meshes and a Contiguous United-States mesh (**CONUS**; featured in Pfister et al. (2020)). While there are dozens of published studies using VR in CESM (e.g., Zarzycki et al., 2014; Rhoades et al., 2016; Gettelman et al., 2017; Burakowski et al., 2019; Bambach et al., 2021), these studies either used development code or collaborated closely with model developers. CESM2.2 is the first code release that contains out-of-the-box VR functionality.

This study compares the representation of Arctic regions using the SE and FV dycores in CESM2.2 (see description below), as these two dycores treat high latitudes (i.e., the pole problem) in different ways. Section 2 documents the grids, dycores, and physical parameterizations used in this study, and also describes the experiments, datasets, and evaluation methods. Section 3 analyzes the results of the experiments, and Section 4 provides a general discussion and conclusions.

## 2 Methods

CESM2.2 is a CMIP6-class (Coupled Model Intercomparison Project Phase 6; Eyring et al., 2016) Earth System Model maintained by the National Center for Atmosphere Re-

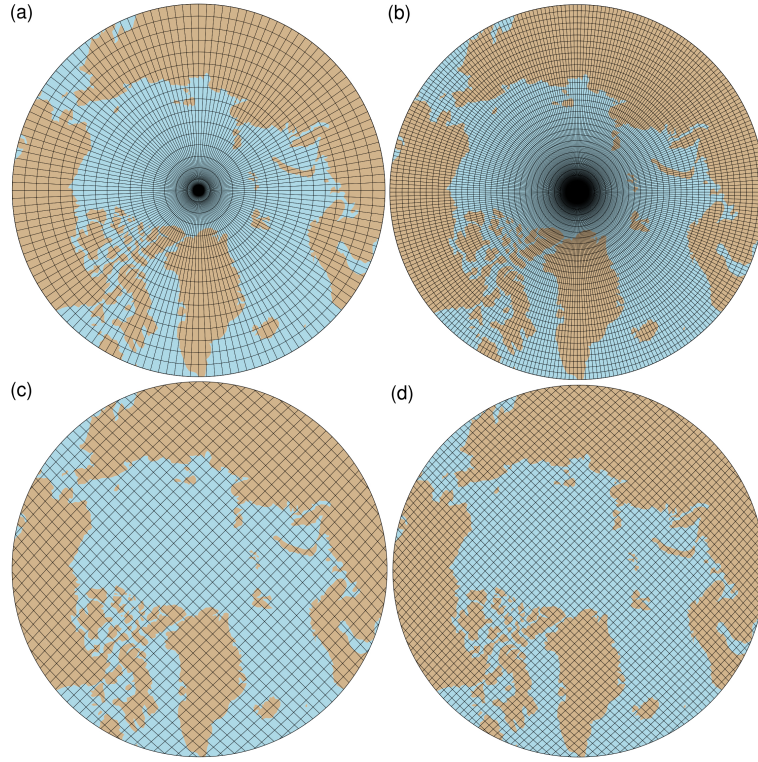


**Figure 1.** Computational grids for the  $1^\circ - 2^\circ$  lat-lon and quasi-uniform unstructured grids in this study. Grids names after Table 1, (a) `f19`, (b) `f09`, (c) `ne30pg2` and (d) `ne30pg3`.

search. CESM2.2 contains sub-component models for the atmosphere, land, ocean, sea-ice, and land-ice, and can be configured to run with varying degrees of complexity. All simulations described in this study use an identical transient 1979–1998 Atmospheric Model Inter-comparison Project (AMIP) configuration, with prescribed monthly sea-surface temperature and sea ice following Hurrell et al. (2008). In CESM terminology, AMIP simulations use the FHIST computational set and run out of the box in CESM2.2. The land-ice component is not dynamically active in FHIST. However, the surface mass balance is computed by the land model before being passed to the land-ice component; FHIST includes the functionality to simulate the surface mass balance of the Greenland Ice Sheet.

## 2.1 Dynamical cores

The atmospheric component of CESM2.2 (Danabasoglu et al., 2020), the Community Atmosphere Model, version 6.3 (CAM6; Gettelman et al., 2019; Craig et al., 2021), supports several different atmospheric dynamical cores. These include dycores on lat-lon grids, such as finite-volume (FV; Lin, 2004) and Eulerian spectral transform (EUL; Collins et al., 2006) models, and dycores built on unstructured grids, including spectral-element (SE; Lauritzen et al., 2018) and finite-volume 3 (FV3; Putman & Lin, 2007) models. This study compares the performance of the SE and FV dycores, omitting the EUL and FV3 dycores. CESM2 runs submitted to CMIP6 used the FV dycore, whereas the SE dycore is often used for global high-resolution simulations (e.g., Small et al., 2014; Bacmeister et al., 2016; Chang et al., 2020) due to its higher throughput on massively parallel systems (Dennis et al., 2012).

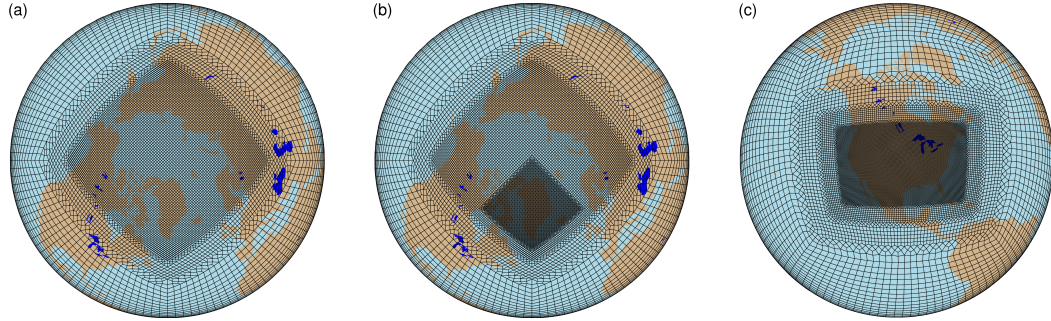


**Figure 2.** Variable-resolution grids available in CESM2.2, (a) **Arctic**, (b) **Arctic – GrIS** and (c) **CONUS**. Note what is shown is the element grid; the computational grid has  $3 \times 3$  independent grid points per element.

### 188      2.1.1 *Finite-volume (FV) dynamical core*

189      The FV dycore integrates the [hydrostatic](#) equations of motion using a finite-volume  
 190      discretization on a spherical lat-lon grid (Lin & Rood, 1997). The 2D dynamics evolve  
 191      in floating Lagrangian layers that are periodically mapped to an Eulerian reference grid  
 192      in the vertical (Lin, 2004). Hyperviscous damping is applied to the divergent modes, and  
 193      is increased in the top few layers (referred to as a *sponge layer*) to prevent undesirable  
 194      interactions with the model top, such as wave reflection (Lauritzen et al., 2011). A polar  
 195      filter damps computational instability due to the convergence of meridians, permit-  
 196      ting a longer time step. It takes the form of a Fourier filter in the zonal direction, with  
 197      the damping coefficients increasing monotonically in the meridional direction (Suarez &  
 198      Takacs, 1995). The form of the filter is designed to slow down the propagation of large  
 199      zonal wave-numbers to satisfy the CFL condition of the shortest resolved wave at some  
 200      reference latitude.

### 201      2.1.2 *Spectral-element (SE) dynamical core*

202      The SE dycore integrates the [hydrostatic](#) equations of motion using a high-order  
 203      continuous Galerkin method (Taylor et al., 1997; Taylor & Fournier, 2010). The com-  
 204      putational domain is a cubed-sphere grid tiled with quadrilateral elements (see Figure 2).  
 205      Each element contains a fourth-order basis set in each horizontal direction, with the so-  
 206      lution defined at the roots of the basis functions, the Gauss-Lobatto-Legendre quadra-  
 207      ture points. This results in 16 nodal points per element, with 12 of the points lying on  
 208      the (shared) element boundary. Communication between elements uses the direct stiff-  
 209      ness summation (Canuto et al., 2007), which applies a numerical flux to the element bound-  
 210      aries to reconcile overlapping nodal values and produce a continuous global basis set.

211      As with the FV dycore, the dynamics evolve in floating Lagrangian layers that are  
 212      subsequently mapped to an Eulerian reference grid. A dry mass vertical coordinate was  
 213      recently implemented for thermodynamic consistency with condensates (Lauritzen et al.,  
 214      2018). The 2D dynamics have no implicit dissipation, and so hyperviscosity operators  
 215      are applied to all prognostic variables to remove spurious numerical errors (Dennis et  
 216      al., 2012). Laplacian damping is applied in the sponge layer.

217      SE is a next generation of dycore, and is less mature than the FV dycore due to  
 218      its shorter history. In CESM2.2, the SE numerics have been enhanced relative to CESM2.0  
 219      to mitigate spurious noise over topography. These algorithmic changes are described in

220 Appendix A. Future versions of CESM will likely continue to include further optimizations  
 221 and enhancements to the (nascent) SE dycore.

222 The SE dycore supports regional grid refinement via its VR configuration, requiring  
 223 two enhancements over quasi-uniform resolution grids. First, as the numerical vis-  
 224 cosity increases with resolution, explicit hyperviscosity relaxes according to the local el-  
 225 ement size, reducing in strength by an order of magnitude per halving of the grid spac-  
 226 ing. A tensor-hyperviscosity formulation is used (Guba et al., 2014), which adjusts the  
 227 coefficients in two orthogonal directions to more accurately target highly distorted quadri-  
 228 lateral elements. Second, the topography boundary conditions are smoothed in a way  
 229 that does not excite grid scale modes, and so the NCAR topography software (Lauritzen  
 230 et al., 2015) has been modified to scale the smoothing radius by the local element size,  
 231 resulting in rougher topography in the refinement zone.

232 When using the SE dycore with quasi-uniform grid spacing, the SE tracer trans-  
 233 port scheme is replaced with the Conservative Semi-Lagrangian Multi-tracer transport  
 234 scheme (CSLAM) (Lauritzen et al., 2017). Atmospheric tracers have large, nearly dis-  
 235 continuous horizontal gradients that are difficult to represent with spectral methods, which  
 236 are prone to oscillatory “Gibbs-ringing” errors (Rasch & Williamson, 1990). CSLAM has  
 237 improved tracer property preservation and accelerated multi-tracer transport. It uses a  
 238 separate grid from the spectral-element dynamics, dividing each element into  $3 \times 3$  con-  
 239 trol volumes with quasi-equal area. The physical parameterizations are computed from  
 240 the state on the CSLAM grid, which has clear advantages over the original SE dycore  
 241 in which the physics are evaluated at Gauss-Lobatto-Legendre points (Herrington et al.,  
 242 2018). CSLAM advection is not an available option in the VR configuration, which in-  
 243 stead uses the standard SE tracer transport scheme with the physics evaluated at Gauss-  
 244 Lobatto-Legendre points.

## 245 2.2 Physical parameterizations

246 All simulations in this study use the CAM6 physical parameterization package (hereafter  
 247 referred to as the *physics*; Gettelman et al., 2019). The physics in CAM6 differs from  
 248 its predecessors through the incorporation of high-order turbulence closure, Cloud Lay-  
 249 ers Unified by Binormals (CLUBB; Golaz et al., 2002; Bogenschutz et al., 2013), which  
 250 jointly acts as a planetary boundary layer, shallow convection, and cloud macrophysics  
 251 scheme. CLUBB is coupled with the MG2 microphysics scheme (Gettelman & Morri-  
 252 son, 2015; Gettelman et al., 2015), which computes prognostic precipitation and uses clas-  
 253 sical nucleation theory to represent cloud ice for improved cloud-aerosol interactions. Deep  
 254 convection is parameterized using a convective quasi-equilibrium mass flux scheme (Zhang  
 255 & McFarlane, 1995; Neale et al., 2008) and includes convective momentum transport (Richter  
 256 et al., 2010). Boundary layer form drag is modeled after Beljaars et al. (2004), and oro-  
 257 graphic gravity wave drag is represented with an anisotropic method informed by the  
 258 orientation of topographic ridges at the sub-grid scale (the ridge orientation is derived  
 259 from a high-resolution, global topography dataset (J. J. Danielson & Gesch, 2011)).

260 Initial simulations with the SE dycore produced weaker shortwave cloud forcing  
 261 relative to the tuned finite-volume dycore in the standard CESM2 configuration. The  
 262 SE dycore in CESM2.2 therefore has two CLUBB parameter changes to provide more  
 263 realistic cloud forcing and top-of-atmosphere radiation balance. We reduced the width  
 264 of the sub-grid distribution of vertical velocity (`clubb_gamma` = 0.308 → 0.270) and  
 265 also reduced the strength of the damping for horizontal component of turbulent energy  
 266 (`clubb_c14` = 2.2 → 1.6) to increase cloudiness. For a description of how CLUBB pa-  
 267 rameters impact the simulated climate, see Guo et al. (2015).

| grid name     | dycore   | $\Delta x_{\text{eq}}$ (km) | $\Delta x_{\text{fine}}$ (km) | $\Delta t_{\text{phys}}$ (s) | cost(25 nodes) | cost(50 nodes) |
|---------------|----------|-----------------------------|-------------------------------|------------------------------|----------------|----------------|
| f19           | FV       | 278                         | -                             | 1800                         | 436.66         | -              |
| f09           | FV       | 139                         | -                             | 1800                         | 1534.57        | 2024.24        |
| ne30pg2       | SE-CSLAM | 167                         | -                             | 1800                         | 1497.26        | 1683.97        |
| ne30pg3       | SE-CSLAM | 111                         | -                             | 1800                         | 1890.48        | 2090.43        |
| ne30pg3*      | SE-CSLAM | 111                         | -                             | 450                          | -              | -              |
| Arctic        | SE       | 111                         | 28                            | 450                          | 15947.41       | 16675.45       |
| Arctic – GrIS | SE       | 111                         | 14                            | 225                          | 40305.03       | 41036.67       |

**Table 1.** Grids and dycores used in this study.  $\Delta x_{\text{eq}}$  is the average equatorial grid spacing,  $\Delta x_{\text{fine}}$  is the grid spacing in the refined region (if applicable), and  $\Delta t_{\text{phys}}$  is the physics time step. FV refers to the finite-volume dycore, SE the spectral-element dycore, and SE-CSLAM the spectral-element dycore with CSLAM tracer advection. We use the ne30pg3 grid for two runs with different values of  $\Delta t_{\text{phys}}$ . The last columns provide the computational costs in core hours per simulated year (CHPSY). The costs are from single month runs using 25 nodes and 50 nodes on the Cheyenne supercomputer (Computational and Information Systems Laboratory, 2017).

268

### 2.3 Grids

We evaluate model simulations on six different grids in this study (Table 1). The FV dycore is run with nominal  $1^{\circ}$  and  $2^{\circ}$  grid spacing, referred to as f09 and f19, respectively (Figure 1a,b). We also run the  $1^{\circ}$  equivalent of the SE-CSLAM grid, referred to as ne30pg3 (Figure 1d), where  $ne$  refers to a grid with  $ne \times ne$  quadrilateral elements per cubed-sphere face, and  $pg$  denotes that there are  $pg \times pg$  control volumes per element for computing the physics. We run an additional  $1^{\circ}$  SE-CSLAM simulation with the physical parameterizations computed on a grid with  $2 \times 2$  control volumes per element, ne30pg2 (Figure 1c; Herrington et al., 2019, note CSLAM is still run on the  $3 \times 3$  control volume grid).

Three VR meshes were developed for the CESM2.2 release to support grid refinement over the Arctic and the United States (Figure 2). This paper serves as the official documentation of these grids. The VR meshes were developed using the software package SQuadgen (<https://github.com/ClimateGlobalChange/squadgen>). The Arctic grid is a  $1^{\circ}$  grid with  $1/4^{\circ}$  regional refinement over the broader Arctic region. The Arctic–GrIS grid is identical to the Arctic grid, but with an additional patch covering the island of Greenland with  $1/8^{\circ}$  resolution. The CONUS grid contains  $1/8^{\circ}$  refinement over the United States, and  $1^{\circ}$  everywhere else. The CONUS grid is not discussed any further in this paper; see Pfister et al. (2020) for simulations with the CONUS grid.

The accuracy of the simulated surface mass balance is expected to be sensitive to grid resolution. Figure 3a shows the average grid spacing over the Greenland Ice Sheet (GrIS hereafter) in all six grids, as well as two grids pertaining to the Regional Atmospheric Climate Model (RACMO; Noël et al., 2018, 2019), which are used for validation purposes in this study (Table 2). The ne30pg2 grid has the coarsest representation with an average grid spacing ( $\Delta x$ ) of  $\Delta x = 160$  km, and the Arctic–GrIS grid has the highest resolution with an average grid spacing of  $\Delta x = 14.6$  km, similar to the 11 km grid spacing of the RACMO2.3 grid. The ne30pg3 grid has an average  $\Delta x = 111.2$  km, substantially coarser than the f09 grid, with an average  $\Delta x = 60$  km. Although ne30pg3 and f09 have similar average grid spacing over the entire globe, and comparable computational costs, the convergence of meridians on the FV grid enhances the resolution over the GrIS. The Arctic grid has an average grid spacing of  $\Delta x = 27.8$  km.

The physics time step depends on the grid resolution. Increased horizontal resolution permits faster vertical velocities that reduce characteristic time scales, so the physics time step is reduced to avoid large time truncation errors (Herrington & Reed, 2018).

302 The **Arctic** and **Arctic – GrIS** grids are run with a  $4\times$  and  $8\times$  reduction in physics  
 303 time step relative to the default 1800 s time step used in the  $1^\circ$  and  $2^\circ$  grids (Table 1).

304 All grids and dycores in this study use 32 hybrid pressure-sigma levels in the ver-  
 305 tical, with a model top of 2 hPa or about 40 km. However, any grid or dycore can in prin-  
 306 ciple be run with a higher model top or finer vertical resolution.

#### 307 2.4 Computational costs

308 The last columns of Table 1 provides cost estimates for the different grids and dy-  
 309 cores. The costs, expressed as core hours per simulated year (CHPSY), are taken from  
 310 single month runs of FHIST, with no i/o, and using 25 nodes (900 tasks) and 50 nodes  
 311 (1800 tasks) on the Cheyenne supercomputer (Computational and Information Systems  
 312 Laboratory, 2017). 25 nodes is on the low side for a typical multi-decadal climate sim-  
 313 ulation at  $1^\circ$  resolution, but it's the largest number of tasks that can be supported by  
 314 the **f19** grid, and we chose to fix the number of tasks across all grids for the purposes  
 315 of comparing their costs. We also provide costs using 50 nodes, excluding **f19**, to pro-  
 316 vide a more practical cost estimate for longer climate integrations. There are probably  
 317 better approaches for comparing costs across different grids and dycores, e.g., holding  
 318 fixed the number of grid columns per task, but it is beyond the scope of this study.

319 The cheapest grid is the **f19** grid at 436.66 CHPSY, as this is the only grid run-  
 320 ning with  $2^\circ$  dynamics. The **f09** grid costs 1534.57 CHPSY using 25 nodes, which is no-  
 321 ticeably cheaper than **ne30pg3** at 1890.48 CHPSY. The **ne30pg2** grid is 20% cheaper than  
 322 the **ne30pg3** grid, in both the 25 node and 50 node runs, consistent with previous es-  
 323 timates (Herrington & Reed, 2018). The FV model is known to be cheaper than SE at  
 324 small core counts, whereas SE is more efficient than FV at large core counts due to its  
 325 improved scalability (Dennis et al., 2005, 2012). In the more conventional 50 node runs,  
 326 **f09** costs are much more similar to **ne30pg3**, due to a 30% cost increase in **f09** relative  
 327 to the 25 node run (Table 1). The **Arctic** grid is an order of magnitude more expen-  
 328 sive than the lat-lon and quasi-uniform grids, at about 16k CHPSY, whereas the **Arctic–**  
 329 **GrIS** grid is a more than twice that (40k CHPSY). Note that all timing numbers are from  
 330 runs without threading. The **f09** grid is the only grid that runs out-of-the-box with thread-  
 331 ing; holding the number of tasks fixed leads to a 4%–6.5% reduction in CHPSY com-  
 332 pared to runs without threading.

#### 333 2.5 Simulated surface mass balance (SMB)

334 CESM simulates the GrIS SMB as the sum of ice accumulation and ice ablation.  
 335 The latter contains contributions from sublimation and liquid runoff from ice melt. Liq-  
 336 uid precipitation and liquid runoff may also contribute to ice accumulation by penetrat-  
 337 ing pore spaces in the snowpack/firn layer and freeze, forming ice lenses. These relevant  
 338 SMB processes are represented by different CESM components, but it is the Commu-  
 339 nity Land Model, version 5 (CLM; Lawrence et al., 2019), that aggregates these processes  
 340 and computes the SMB.

341 CLM runs on the same grid as the atmosphere, and uses a downscaling technique  
 342 to account for sub-grid variability in SMB. In short, the ice sheet patch in a CLM grid  
 343 cell is subdivided into 10 elevation classes (ECs), each with a distinct surface energy bal-  
 344 ance and SMB. The area fraction of each EC is computed from the CISM initial con-  
 345 ditions, which are based on a high-resolution dataset of the observed, modern extent and  
 346 thickness of the GrIS (Morlighem et al., 2014). Note that for configurations with a dy-  
 347 namically active ice sheet, the area fractions are continuously updated throughout the  
 348 run to reflect the evolving ice sheet geometry in CISM. The near-surface air tempera-  
 349 ture, humidity, and air density are calculated for each EC using an assumed lapse rate  
 350 and the elevation difference from the grid-cell mean. Precipitation from CAM is repar-

| data product     | years used in this study | resolution | citation              |
|------------------|--------------------------|------------|-----------------------|
| ERA5             | 1979-1998                | 1/4°       | Copernicus (2019)     |
| CERES-EBAF ED4.1 | 2003-2020                | 1°         | Loeb et al. (2018)    |
| CALIPSO-GOCCP    | 2006-2017                | 1°         | Chepfer et al. (2010) |
| RACMO2.3         | 1979-1998                | 11 km      | Noël et al. (2015)    |
| RACMO2.3p2       | 1979-1998                | 5.5 km     | Noël et al. (2019)    |

**Table 2.** Description of validation datasets used in this study.

titioned into solid or liquid based on the surface temperature of the EC; precipitation falls as snow for temperatures between  $T < -2^{\circ}$  C, as rain for  $T > 0^{\circ}$  C, and as a linear combination of rain and snow for temperatures between  $-2^{\circ}$  C and  $0^{\circ}$  C.

Changes in ice depth, not snow depth, count toward the SMB. Snow accumulation in each EC is limited to a depth of 10 m liquid water equivalent. Any snow above the 10 m cap contributes towards ice accumulation, and refreezing of liquid water within the snowpack is an additional source of ice. Surface ice melting (after melting of the overlying snow) yields a negative SMB. Integrating over all ECs, weighting by the area fractions, provides a more accurate SMB than would be found using the grid-cell mean elevation. For a more detailed description of how the SMB is computed in CESM, we refer the reader to Lipscomb et al. (2013); Sellevold et al. (2019); van Kampenhout et al. (2020); Muntjewerf et al. (2021).

Since snow in the accumulation zone must reach the cap to simulate a positive SMB, the snow depths on the VR grids were spun up by forcing CLM in standalone mode, cycling over data from a 20-year Arctic FHISt simulation for about 500 years. The 1°–2° lat-lon and quasi-uniform unstructured grids are initialized with the SMB from an existing f09 spun-up initial condition.

## 2.6 Validation Datasets

We use several validation datasets (Table 2) to assess the performance of the simulations. The ERA5 reanalysis product (Copernicus, 2019) is used for validating the large-scale circulation and extreme precipitation events. Clouds and radiation fields are validated using remote sensing products, the CERES-EBAF ED4.1 (Loeb et al., 2018) and the CALIPSO-GOCCP (Chepfer et al., 2010) datasets, respectively.

SMB datasets are gathered from multiple sources. RACMO, version 2.3 11km (RACMO23; Noël et al., 2015) and version 2.3p2 5.5km (RACMO2.3p2; Noël et al., 2018, 2019) are RCM simulations targeting Greenland, forced by ERA renalyses products at the domain's lateral boundaries. The RACMO simulations have been shown to perform skillfully against observations and are often used as modeling targets (e.g., Evans et al., 2019; van Kampenhout et al., 2020). The RACMO datasets are used along with the CERES-EBAF product to validate the radiative fluxes around Greenland.

In-situ SMB (snow pit and ice cores) and remote sensing datasets (e.g., IceBridge radar accumulation dataset) are maintained in The Land Ice Verification and Validation toolkit (LIVVkit), version 2.1 (Evans et al., 2019). However, these point-wise measurements are difficult to compare to model output spanning several different grids, especially since the SMB from each elevation class is not available from the model output. We used a nearest-neighbor technique for an initial analysis, which showed that the model biases are similar to those computed using the RACMO datasets. Because of the uncertainty of comparing gridded fields to point-wise measurements, and the lack of information added with regard to model biases, we omitted these datasets from our analysis.

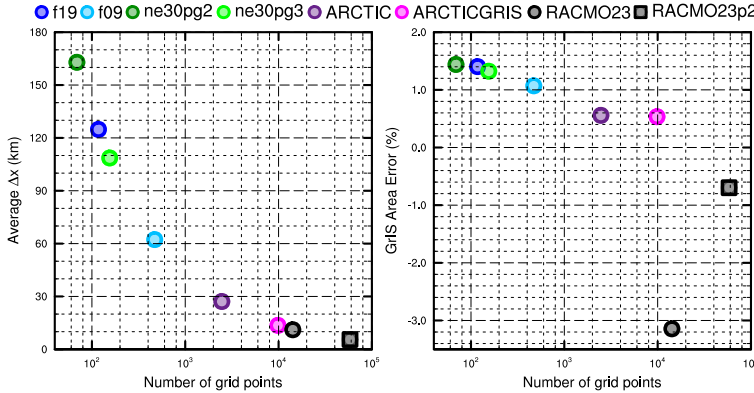


**Figure 3.** The spatial properties of the GrIS as represented by different grids in this study. (Left) GrIS area error, computed as the relative differences from a 4-km dataset used to create the CESM ice masks, (right) approximate average grid spacing over GrIS.

## 390 2.7 SMB Analysis

We seek to integrate SMB components over a GrIS ice mask and to diagnose their contributions to the GrIS mass budget. However, the ice masks vary across the grids, especially in comparison to the RACMO3.2 ice mask, whose total area is about 3% less than that of the reference dataset (i.e., the GrIS initial conditions in CISM; Figure 3b). CLM's dataset creation tool generates the model ice mask by mapping the reference dataset to the target grid using the Earth System Modeling Framework (ESMF) first-order conservative remapping algorithm (Team et al., 2021). The figure suggests that the mapping errors are less than 1.5% across the CESM2.2 grids. The area errors in Figure 3b may seem small, but even 1–2% area differences can lead to large differences in integrated SMB (Hansen et al., 2022).

We have taken a common-ice-mask approach by mapping all model fields to the lowest-resolution grids, i.e., the f19 and ne30pg2 grids, and integrating over these low-resolution ice masks. The use of low-resolution common ice masks is a conservative decision, and is justified because we seek to use first-order remapping algorithms to map fields to the common ice mask, which is not generally reliable when mapping to a higher-resolution grid than the source grid. We use two remapping algorithms: ESMF first-order conservative and the TempestRemap (Ullrich & Taylor, 2015) high-order monotone algorithm. Since mapping errors are sensitive to grid type, we evaluate all quantities on both common ice masks, the f19 and ne30pg2 masks. Thus, we evaluate an integrated quantity on a given grid up to four times to estimate the uncertainty due to differences in grid type and remapping algorithms.

The SMB is expressed in a form that is agnostic of water phase, a total water mass balance, to facilitate comparisons across different grids with different ice masks and to increase consistency with the variables available in the RACMO datasets. The SMB for total water can be expressed as:

$$SMB = accumulation + runoff + evaporation + sublimation, \quad (1)$$

where all terms have consistent sign conventions (positive values contribute mass, and negative values reduce mass). The accumulation source term refers to the combined solid and liquid precipitation, runoff refers to the liquid water sink, and evaporation/sublimation is the vapor sink. Since the runoff term aggregates many processes, we isolate the melting contribution by also tracking the combined melt of snow and ice.

421      The total water SMB (equation 1) is different from the SMB internally computed  
 422      by CLM and described in section 2.5, which only tracks ice mass. We do not use CLM's  
 423      internally computed SMB in this study. Rather, we utilize the components of the inter-  
 424      nally computed SMB to construct the total water SMB.

425      We consider two approaches for mapping and integrating the SMB components over  
 426      the common ice masks:

- 427      1. Map the grid-cell mean quantities to the common grid, and integrate the mapped  
   428      fields over the common ice masks.
- 429      2. Map the patch-level quantities (i.e., the state over the ice fractional component  
   430      of the grid cell) to the common grid, and integrate the mapped fields over the com-  
   431      mon ice masks.

432      Note that we are mapping to low-resolution grids that have larger GrIS areas than  
 433      the source grids (Figure 3b). Since the components of equation 1 are not confined to the  
 434      ice mask, method 1 reconstructs the SMB over the portion of the common ice mask that  
 435      is outside the ice mask on the source grid. While this may be a an acceptable way to re-  
 436      construct the mass source terms over different ice masks, ice melt is zero outside the source  
 437      ice mask, and so method 1 will underestimate the mass sink term. This underestima-  
 438      tion is systematic in method 2, where all variables are exclusive to the ice mask; map-  
 439      ping to a lower-resolution grid will dilute a field of non-zero values over the ice mask with  
 440      a field of zeros outside the ice mask. However, patch-level values for processes exclusive  
 441      to the ice mask (e.g., ice melt) will on average have larger magnitudes than the grid-mean  
 442      quantities used in method 1.

443      The different error characteristics of the two methods are used to [further](#) diversify  
 444      the ensemble. Each of the four regridding combinations (with conservative and high-order  
 445      remapping to the f09 and ne30pg2 grids) are repeated with each method, resulting in  
 446      (up to) eight values for each integrated quantity. Unfortunately, the patch-level values  
 447      of evaporation/sublimation are not available from the model output, and we estimate  
 448      their contribution by zeroing out the field for grid cells that have no ice, prior to map-  
 449      ping to the common ice mask. This will degrade the SMB estimates using method 2, but  
 450      we are more interested in characterizing the behavior of individual processes across grids  
 451      and dycores, expressed as the components of the SMB, rather than the SMB itself.

### 452      3 Results

#### 453      3.1 Tropospheric temperatures

454      Before delving into the simulated Arctic climate conditions, we assess the global  
 455      mean differences between the various grids and dycores. Figure 4 shows 1979-1998 an-  
 456      nual mean, zonal mean height plots expressed as differences between [1°–2° lat-lon](#) and  
 457      [quasi-uniform unstructured](#) grids and dycores. The f09 grid is warmer than the f19 grid,  
 458      primarily in the mid-to-high latitudes throughout the depth of the troposphere. This is  
 459      a common response to increasing horizontal resolution in GCMs (Pope & Stratton, 2002;  
 460      Roeckner et al., 2006). Herrington and Reed (2020) have shown that this occurs in CAM  
 461      due to higher resolved vertical velocities which, in turn, generate more condensational  
 462      heating in the CLUBB macrophyiscs. The right panel in Figure 4a supports this inter-  
 463      pretation, showing an increase in the climatological CLUBB heating at all latitudes in  
 464      the f09 grid, but with the largest increase in the mid-latitudes.

465      As the SE dycore is less diffusive than the FV dycore, the resolved vertical veloc-  
 466      ities are larger in the SE dycore, and so the ne30pg3 troposphere is modestly warmer  
 467      than f09 (Figure 4b). The stratosphere responds differently, with ne30pg3 much cooler  
 468      than f09 in the mid-to-high latitudes. Figure 4c also shows small temperature differences

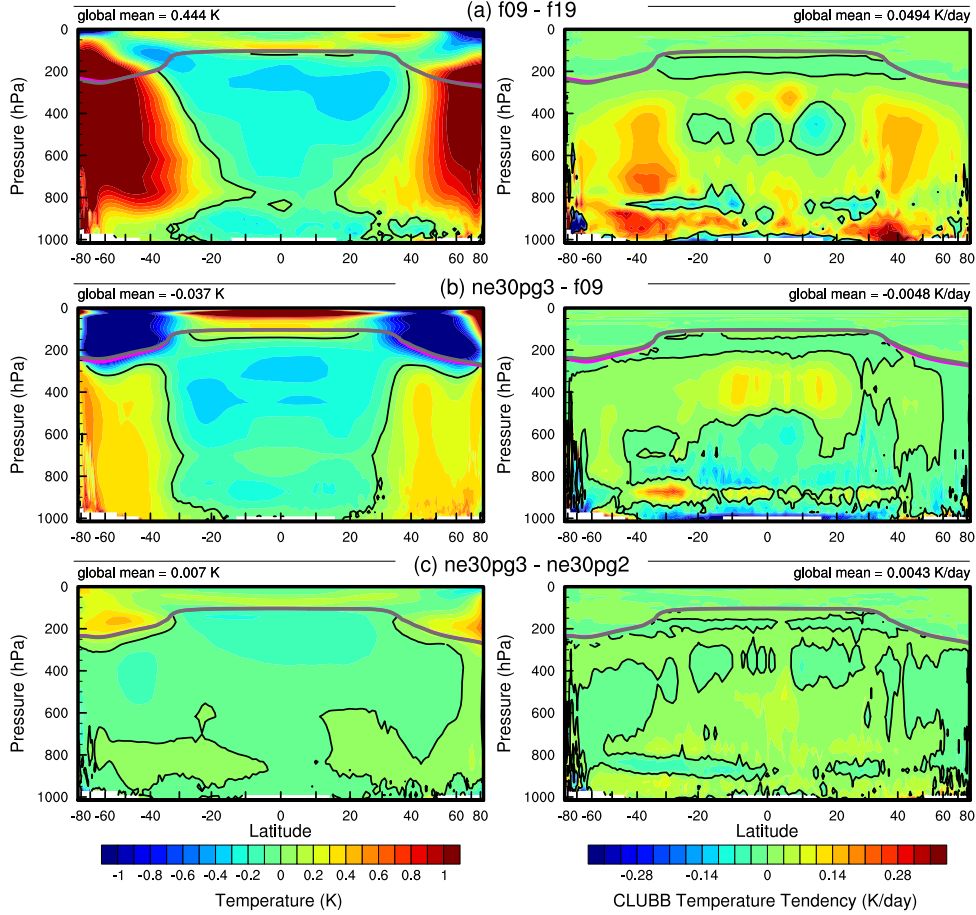


**Figure 4.** 1979–1998 annual mean temperature (left column) and CLUBB temperature tendencies (right column) in zonal mean height space, expressed as differences between the various  $1^{\circ} - 2^{\circ}$  grids. The thick grey and magenta lines are the tropopause for the control run and the test run, respectively.

between ne30pg3 and ne30pg2, with ne30pg3 slightly warmer near the tropopause at high latitudes. This is consistent with the similar climates found for these two grids by Herrington et al. (2019).

Comparing the VR grids to the lat-lon and quasi-uniform grids is complicated because we simultaneously increase the resolution and reduce the physics time-step, both of which influence the solution (Williamson, 2008). We therefore run an additional ne30pg3 simulation with the shorter physics time step used in the Arctic grid (450 s), referred to as ne30pg3\* (Table 1). Figure 5a shows the difference between ne30pg3\* and ne30pg3 for climatological summer temperatures in zonal-mean height space. The troposphere is warmer with the reduced time step, and the mechanism is similar in that the shorter time step increases resolved vertical velocities (not shown) and CLUBB heating (right panel in Figure 5a). Figure 5b shows the difference in climatological summer temperature between the Arctic grid and the ne30pg3\* grid. With the same physics time step, the greater condensational heating and warmer temperatures are confined to the refined Arctic region.

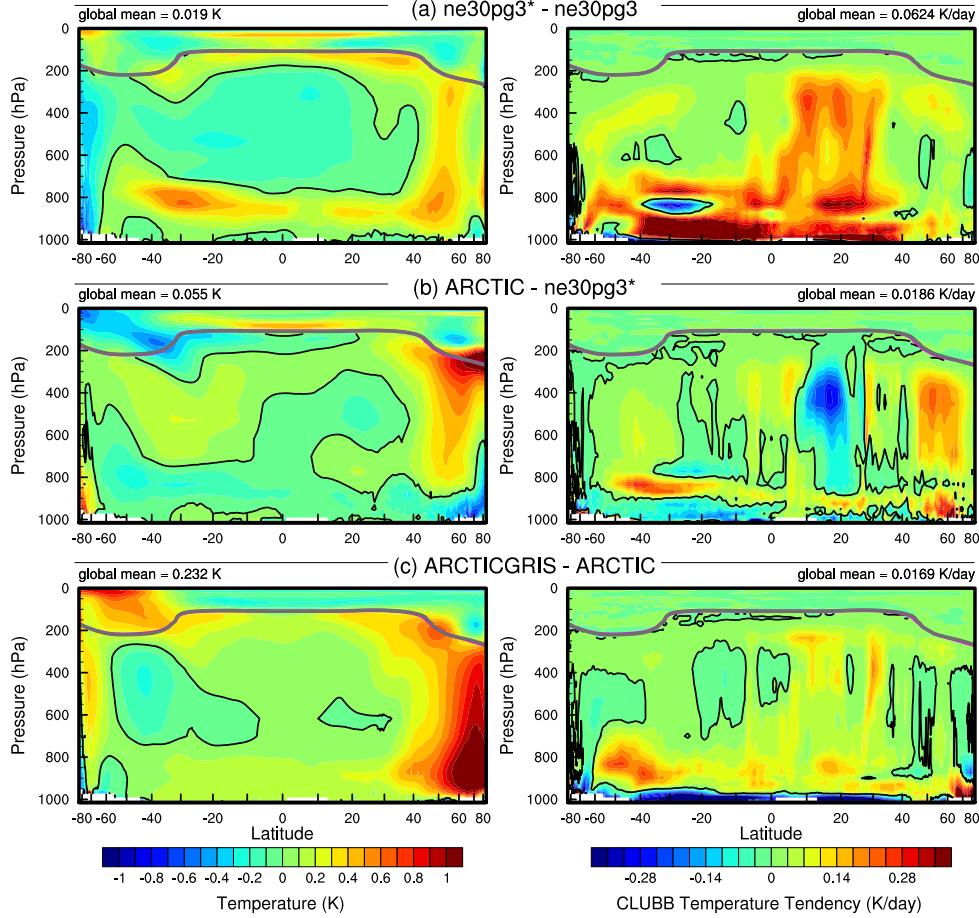


**Figure 5.** As in Figure 4 but for the short-time-step experiment and the VR grids. The fields plotted are for the climatological northern hemisphere summer. We focus on summer because that is when the resolution response is largest, and the refined regions are located in the northern hemisphere.

Figure 5c shows that the `Arctic-GrIS` grid is much warmer than the `Arctic` grid in the Arctic summer. This may be due, in part, to the shorter physics time step, but the temperature response is too large to be explained by enhanced condensational heating from CLUBB alone. This summer warming appears to be a result of variations in the stationary wave pattern, with a swath of anomalous southerly winds to the west of Greenland (not shown). This dynamic response is interesting, because other than the physics time step, the only difference between the `Arctic-GrIS` and `Arctic` runs is the doubling of resolution over Greenland. This behavior will be explored further in a future study.

Keeping our focus on the Arctic region, and in particular Greenland, it is useful to understand summer temperature biases due to their control on ice and snow melt over the GrIS (Ohmura, 2001). Figure 6 shows the 1979–1998 lower troposphere summer temperature bias relative to ERA5, computed by equating a layer mean virtual temperature with the 500–1000 hPa geopotential thickness. The results are consistent with the zonal mean height plots; increasing resolution from f19 to f09 warms the climate, and the 1° SE grids are warmer than the FV grids. The FV summer temperatures are persistently

500 colder than ERA5, whereas the  $1^\circ$  SE grids are not as cold, and are actually warmer than  
 501 ERA5 at high-latitudes, north of  $75^\circ$ . All grids show a north-south gradient in bias over  
 502 Greenland, with the summer temperature bias more positive for the northern part of the  
 503 ice sheet. This pattern is also evident in the near surface temperature bias over Green-  
 504 land (not shown).

505 The **Arctic** grid has summer temperatures similar to the  $1^\circ$  SE grids, but is slightly  
 506 warmer over northern Eurasia and the North Pole (Figure 6). An anomalous cooling patch  
 507 forms to the west of Greenland, centered over Baffin Island. The **Arctic – GrIS** grid  
 508 is warmer than the **Arctic** grid over most of the Arctic, but with a similar spatial pat-  
 509 tern of summer temperature bias.

510 Some of these temperature differences may be related to differences in summer cloudi-  
 511 ness. Figure 7 shows the summer shortwave cloud forcing bias in the six runs, using the  
 512 CERES product. Shortwave cloud forcing quantifies the impact of clouds on shortwave  
 513 radiation, taken as the difference between all-sky and clear-sky shortwave radiative fluxes  
 514 at the top of the atmosphere. A negative bias corresponds to excessive reflection and cool-  
 515 ing. The [lat-lon and quasi-uniform](#) grids have similar biases, with the clouds reflecting  
 516 20–40 W/m<sup>2</sup> too much shortwave radiation over a wide swath of the Arctic, primarily  
 517 the land masses. There is also a halo of positive bias (clouds not reflective enough) around  
 518 the ocean perimeter of Greenland. The **Arctic** grid has much smaller cloud forcing bi-  
 519 ases over the Arctic land masses, but is still too reflective over Alaska, the Canadian Archipelago,  
 520 and parts of Eurasia. Compared to the **Arctic** grid, the **Arctic–GrIS** grid vastly re-  
 521 duces the cloud forcing bias over Eurasia, and also improves the bias over North Amer-  
 522 ica. In both VR grids, the halo of positive shortwave cloud forcing bias around the perime-  
 523 ter of Greenland is absent.

524 The summer cloud forcing biases are consistent with the summer temperature bi-  
 525 ases in Figure 6 – regions where clouds are too reflective coincide with regions that are  
 526 too cold. While we have not quantified the contribution of cloud biases to the cooler Arc-  
 527 tic temperatures, shortwave radiation is a crucial component of the Arctic energy bud-  
 528 get during summer. The shortwave cloud forcing biases are on the order of 10 W/m<sup>2</sup>,  
 529 which is a significant fraction of the total absorbed shortwave [radiation](#) during Arctic  
 530 summer (Serreze et al., 2007) and is therefore likely a factor contributing to the cooler  
 531 temperatures.

### 532 3.2 Clouds and precipitation over Greenland

533 In addition to summer temperatures, shortwave radiation is an important deter-  
 534 minant of snow and ice melt. Figure 8 shows the summer incident shortwave radiation  
 535 bias at the surface over Greenland and surrounding seas. The top panel shows the bias  
 536 relative to the RACMO2.3p2 dataset, and the middle panel relative to the CERES dataset.  
 537 The halo of excessive incident shortwave radiation around the coasts of Greenland is ap-  
 538 parent for both datasets in relation to the coarser grids, consistent with the shortwave  
 539 cloud forcing biases in Figure 7.

540 The ice sheet interior receives too little shortwave radiation in the coarser grids.  
 541 On the VR grids, both the interior shortwave deficit and the excessive shortwave around  
 542 the ocean perimeter are improved. This suggests that the coarse grid clouds are too thick  
 543 in the interior of Greenland and too thin around the perimeter, which is consistent with  
 544 the total summer cloud fraction bias, computed from the CALIPSO cloud dataset and  
 545 shown in the bottom panel of Figure 8. Note that total cloud fraction characterizes the  
 546 cloud field at all vertical levels, and attenuates the changes arising from any single layer  
 547 due to the occurrence of overlapping clouds at other levels. The VR grids exhibit an over-  
 548 all improvement in total cloud fraction bias, relative to the coarse grids.

| grid name     | accumulation  | total melt      | runoff          | sublimation   | SMB           |
|---------------|---------------|-----------------|-----------------|---------------|---------------|
| RACMO         | 681.7 (733.5) | -318.6 (-436.4) | -189.1 (-258.5) | -34.5 (-38.8) | 458.1 (436.2) |
| ne30pg2       | 1007. (973.4) | -519.9 (-647.3) | -381.9 (-347.0) | -33.9 (-32.1) | 591.2 (594.3) |
| ne30pg3       | 931.0 (909.3) | -540.8 (-686.7) | -375.8 (-330.1) | -34.1 (-32.6) | 521.2 (546.6) |
| f19           | 884.9 (913.5) | -414.0 (-546.5) | -284.0 (-284.3) | -36.5 (-37.5) | 564.4 (591.7) |
| f09           | 873.9 (882.1) | -389.1 (-482.3) | -256.1 (-212.3) | -37.3 (-37.4) | 580.5 (632.4) |
| Arctic        | 784.1 (818.6) | -335.5 (-436.8) | -215.8 (-194.2) | -42.4 (-43.9) | 526.0 (580.5) |
| Arctic – GrIS | 693.8 (747.3) | -437.3 (-610.4) | -276.8 (-307.8) | -48.1 (-51.8) | 369.0 (387.7) |

**Table 3.** 1979-1998 surface mass balance of the Greenland Ice Sheet in Gt/yr. Values shown are using the common ice mask approach described in the methods section, whereas values in parentheses are from integrating over the native grid and ice mask.

The top panel of Figure 9 shows the annual climatological mean precipitation bias over the GrIS, expressed as the fractional difference from the RACMO2.3p2 solution. The coarse  $1^\circ - 2^\circ$  grids have large, positive biases centered over the southern dome. The Arctic grid reduces this bias substantially, and the Arctic–GrIS grid reduces it further, with precipitation centers migrating from the interior toward the margins.

The more accurate representation of orographic precipitation in the VR grids is consistent with the cloud and radiation biases, cf. Figures 7, 8, and 9. The agreement of the cloud, radiation and precipitation biases in and around Greenland from multiple independent datasets indicates that the biases are a robust feature of the coarser grids. The reduced biases in the VR grids suggest that the deficiencies of the coarse grids are due to insufficient horizontal resolution, consistent with previous findings that coarse GCMs have large, positive precipitation biases over Greenland (Pollard & Groups, 2000; Van Kamphout et al., 2019).

### 3.3 Greenland surface mass balance

Table 3 shows the 1979-1998 climatological SMB components for each grid, compared with RACMO. The values in the table are averages over the ensemble of mapping methods to the common ice masks described in section 2.7, and the RACMO values refer to the average of both RACMO ensembles. Table 3 also contains (in parenthesis) the SMB components derived from evaluating the integrals on each model’s native grid and ice mask. Of note is the large reduction in melt rates compared to the values computed on the native grid, illustrating the dissipation of this quantity discussed in section 2.7. For integrated precipitation, the differences between the native and common ice mask approaches are much smaller, since the combined solid/liquid precipitation rates are not directly tied to the ice mask.

The coarse grids are characterized by too much precipitation and too much melting and runoff, compared with RACMO. The total SMB on coarse grids therefore has smaller errors than the individual components (Table 3), because large errors in the source and sink terms offset one another when added together. Such compensating errors underline the importance of understanding the extent to which a model is getting the right SMB for the right reasons.

Figure 10 shows time series of annually integrated precipitation and snow/ice melt over the GrIS for the various different grids and dycores, and RACMO in black. The 1979-1998 climatological mean values from Table 3 are shown as circles on the right side of the panels. The  $1^\circ - 2^\circ$  lat-lon and quasi-uniform grids have positive precipitation biases, whereas the VR grids have the smallest biases, with precipitation comparable to RACMO. The f19 and f09 grids perform similarly, with +110 Gt/yr bias, whereas ne30pg3 is biased by about +165 Gt/yr and ne30pg2 by +230 Gt/yr.

586 The combined annual snow/ice melt shown in the bottom panel of Figure 10 indicates  
 587 that the **Arctic** grid simulates the most realistic melt rates, with the other grids  
 588 having more melt than RACMO. The **Arctic–GrIS** grid over-predicts melting by about  
 589 125 Gt/yr. This is likely due to an anomalously warm lower troposphere during the summer,  
 590 relative to the **Arctic** run (Figure 6). The **f19** and **f09** melting rates are improved  
 591 over **Arctic–GrIS**, overestimating melt by only 70–90 Gt/yr. The SE grids have the  
 592 largest positive melt bias, between 200–220 Gt/yr.

593 To illustrate the regional behavior of the SMB components, Figure 11 shows the  
 594 precipitation and combined snow/ice melt integrated over the basins defined by Rignot  
 595 and Mouginot (2012). The uncertainty due to differences in basin area is larger than for  
 596 GrIS-wide integrals, owing to the differences in basin boundaries on the common ice masks,  
 597 which are shown in the **f19** and **ne30pg2** panels of Figure 9. Nonetheless, the regional  
 598 totals in Figure 11 correctly show the southeast and southwest basins have the most accu-  
 599 mulation. In all basins, accumulation decreases monotonically with increasing grid res-  
 600 olution, though with some exceptions. The **Arctic – GrIS** grid simulates less precipi-  
 601 tation than RACMO in the central-east and southeast basins, and is closest of all grids  
 602 to RACMO in the large southwest basin.

603 The basin-integrated melt rates in Figure 11 depend on the dycore. The **quasi-uniform**  
 604 **SE** grids have the largest positive biases in all basins. The **Arctic–GrIS** grid is a close  
 605 second, while the FV grids have systematically **smaller melt-rates and melt-rate biases**.  
 606 The “second-place” standing of **Arctic–GrIS** is somewhat unexpected, as this grid has  
 607 the warmest lower-troposphere summer temperatures (Figure 6) and greatest incident  
 608 shortwave radiation (Figure 8), yet it has less melting than the **quasi-uniform** **SE** grids.

609 Lower troposphere temperature is not a strict proxy for melting; e.g., it may not  
 610 capture microclimate effects as a result of a better representation of the low-elevation  
 611 ablation zones. The Positive Degree-Day temperature-based melt index (PDD; Braith-  
 612 waite, 1984), which accumulates the near-surface temperature in  $^{\circ}\text{C}$  for days with tem-  
 613 perature above freezing, is a more accurate proxy for melting. PDD is nonlinear in mean  
 614 monthly temperature (Reeh, 1991). We compute PDD from monthly mean 2-meter tem-  
 615 perature using the method of Calov and Greve (2005), assuming a fixed monthly mean  
 616 standard deviation of  $3^{\circ}\text{C}$  and a degree-day factor of  $5 \text{ mm d}^{-1} ^{\circ}\text{C}^{-1}$ . **This specific degree-**  
 617 **day factor lies between typical values reported for snow and ice, in order to easily ap-**  
 618 **ply the PDD method to estimate the combined snow and ice melt.**

619 Figure 11c shows the basin-integrated PDD melt estimate. In the large southeast  
 620 and southwest basins (and all the other western basins), the **ne30pg3** grid has larger PDD-  
 621 based melt than the **Arctic–GrIS** grid. The FV grids also have large PDD-based melt  
 622 in the southwest basin, relative to **Arctic–GrIS**. The PDD plots indicate that the re-  
 623 lationship between temperature and melt is not well approximated by the summer lower-  
 624 troposphere temperatures in Figure 6.

625 The bottom panel of Figure 9 presents the biases in the combined ice/snow melt  
 626 as map plots. These plots show that the largest melt biases are on the southeast and north-  
 627 west coasts, where large coarse-grid cells overlap with the ocean. One possibility is that  
 628 these problematic grid cells are situated at lower elevations than the true ice sheet sur-  
 629 face, leading to a warm bias and too much melt. Figure 12 shows the representation of  
 630 the ice sheet surface along two transects on the different grids, compared to the high-  
 631 resolution dataset used to generate CAM topographic boundary conditions (J. Daniel-  
 632 son & Gesch, 2011; Lauritzen et al., 2015). The two transects are shown in Figure 9: the  
 633 east-west “K-transect” in southwest Greenland and a transect extending from the cen-  
 634 tral dome down to the Kangerlussuaq glacier on the southeast coast. The  $1^{\circ}$ – $2^{\circ}$  grids  
 635 are noticeably coarse, with only a handful of grid cells populating the transect. The **f09**  
 636 grid is a bit of an exception since the grid cells narrow in the zonal direction at high lat-  
 637 itudes, and so a larger number of grid cells fit into the east-west transects. The VR grids

638 more accurately reproduce the steep margins of the ice sheet, capturing the characteristic  
 639 parabolic shape of the GrIS margin.

640 The transects in Figure 12 show that the ice sheet surface on the coarse grids is  
 641 not systematically lower than the true surface in ablation zones. Rather, the smoothing  
 642 and flattening of the raw topography, necessary to prevent the model from exciting  
 643 grid-scale numerical modes, causes the lower-elevation ablation zones to extend beyond  
 644 the true ice sheet margin, causing the modeled ablation zones (which must reside within  
 645 the ice sheet mask) to be elevated relative to the actual ice surface. The f19 grid has  
 646 both the smoothest topography and the flattest ice sheet since its dynamics are coars-  
 647 est, whereas the f09, ne30pg2 and ne30pg3 grids have similar dynamical resolution and  
 648 use identical smoothing. This suggests that coarser models will tend to elevate the ab-  
 649 lation zones **relative to where they should be, which may be expected to cause anomalous (adiabatic) cooling and** depressed melt rates, but this is opposite the melt bias that  
 650 occurs in the coarse grid simulations.  
 651

652 Figure 12 also shows the ice margin boundary, illustrating that the ablation zone  
 653 lies in a narrow horizontal band where the ice sheet rapidly plunges to sea-level. Due to  
 654 this abrupt transition, coarse grids will commonly represent the ablation zone with grid  
 655 cells containing mixtures of ice-covered and ice-free regions. We hypothesize that coarser  
 656 models have larger melt biases because summer melting is confined to these mixed ice/land/ocean  
 657 grid cells. CLM deals with land heterogeneity in a complex and sophisticated manner,  
 658 but CAM only sees the homogenized state after **area** averaging over the sub-grid mix-  
 659 ture. Thus, warm ice-free land patches in a grid cell may unduly influence the climate  
 660 over the entire grid cell, causing a warm bias over the ice-covered patch **and more melt-**  
 661 **ing.**

662 Figure 13 shows the mean melt bias, relative to both RACMO datasets, condition-  
 663 ally sampled based on grid cell ice fraction in the GrIS region. Errors are computed af-  
 664 ter mapping the melt rates to the common ice masks using different methods, described  
 665 in section 2.7. The grid cell ice fractions therefore pertain to ice fractions on the low-  
 666 resolution common ice masks. Also shown are the  $\pm 1$  standard deviation of the biases  
 667 for each bin. The figure shows that coarser grids can be characterized by a monotonic  
 668 increase in melt bias as the grid cell ice fraction decreases. The VR grids have the small-  
 669 est melt biases for small grid cell ice fractions (less than 50%), the **quasi-uniform SE** grids  
 670 and f19 have the largest melt biases and the f09 grid melt biases lie between these two  
 671 cases. Figure 13 generally supports our hypothesis that the prevalence of mixed-grid cells  
 672 in the ablation zone of coarse grids is responsible for their large melt bias.

673 Another potential factor in explaining the differences across the various grids and  
 674 dycores is the surface albedo. Bare ice has a lower albedo than snow, so it's reasonable  
 675 to speculate whether the large melt biases in the coarse grid simulations are in part due  
 676 to more frequent bare ice exposure. One logical pathway to more bare ice exposure is  
 677 related to the precipitation and cloud biases. As the coarser models accumulate too much  
 678 precipitation in the GrIS interior, the coastal ice margins receive too little snow, which  
 679 can be more easily melted away to expose the underlying glacial ice. Figure 14 shows  
 680 maps of summer albedo biases in the simulations, relative to the RACMO2.3p2 and CERES-  
 681 EBAF datasets. The surface albedo is diagnosed from the incident and net shortwave  
 682 radiative fluxes at the surface. The lat-lon and quasi-uniform grids all have anomalously  
 683 low albedo around the coasts in the southeast and northwest regions of the GrIS, which  
 684 coincides with regions of anomalously low cloud cover and precipitation. In the VR sim-  
 685 ulations, the low albedo biases are alleviated to a large extent.

686 In light of these albedo results, one may interpret Figure 13 differently. That there  
 687 are larger melt biases for grid cells with only partial ice cover, may have less to do  
 688 with the partial ice cover and more to do with the enhanced bare ice exposure in the coarser

689 grids. Further experimentation is required to tease out the relative contributions of these  
 690 two processes.

### 691 3.4 Precipitation extremes

692 Synoptic storms are tracked using TempestExtremes atmospheric feature detec-  
 693 tion software (Ullrich et al., 2021). As the **Arctic** grid contains  $1/4^\circ$  refinement north  
 694 of about  $45^\circ$  latitude, the storm tracker is applied to this region for the **Arctic** and **ne30pg3**  
 695 runs to identify differences in storm characteristics due to horizontal resolution.

696 Figure 15 shows monthly PDF ([probability density function](#)) of the precipitation  
 697 rates associated with storms. The PDFs are constructed by sampling all the precipita-  
 698 tion rates within  $30^\circ$  of the storm center, for each point on the storm track and for all  
 699 storms. The PDFs are evaluated on an identical composite grid for all runs, and so storm  
 700 statistics are not impacted by differences in output resolution. The **Arctic** run has larger  
 701 extreme precipitation rates compared to **ne30pg3** in every month, but the increase is great-  
 702 est in the summer months, which coincides with the most extreme events of the year.  
 703 This is primarily due to increased resolution and not the reduced physics time step; the  
 704 **ne30pg3\*** run only marginally increases the extreme precipitation rates compared with  
 705 **ne30pg3** (Figure 15).

706 The extreme precipitation rates in the **Arctic** run are closer than **ne30pg3** to the  
 707 ERA5 reanalysis (Figure 15). It is difficult to know how much the extreme precipitation  
 708 rates in ERA5 are constrained by data assimilation, or whether these precipitation rates  
 709 are due to using a similar  $1/4^\circ$  model as the **Arctic** grid. However, it is well documented  
 710 that  $1/4^\circ$  models are more skillful at simulating extreme events (Bacmeister et al., 2013;  
 711 Obrien et al., 2016). A more realistic representation of extreme precipitation events is  
 712 an additional benefit of the VR grids.

## 713 4 Conclusions

714 Running CESM2.2 in an AMIP-style configuration, we have evaluated six grids from  
 715 two dynamical cores for their performance over the Arctic and in simulating the GrIS  
 716 SMB. The  $1 - 2^\circ$  finite-volume grids have enhanced resolution over polar regions due  
 717 to their convergence of meridian lines, although a polar filter is used to prevent spuri-  
 718 ous atmospheric features from forming in these regions. SE grids comparable to the res-  
 719 olution of the FV grids have an isotropic grid structure where the grid resolution is sim-  
 720 ilar over the entire model domain. We developed two VR grids and introduced them into  
 721 CESM2.2 as part of this work. Both use the SE dycore; the **Arctic** grid has  $1/4^\circ$  refine-  
 722 ment over the broader Arctic, whereas the **Arctic – GrIS** grid is identical except for  
 723 a  $1/8^\circ$  patch of refinement over Greenland. A third VR grid, **CONUS**, [with  \$1/8^\circ\$  refine-](#)  
 724 [ment over the US](#), has also been made available in CESM2.2.

725 In general, the FV grids have colder summer temperatures over the Arctic com-  
 726 pared with the SE grids (including the VR grids). The cloud biases in all the [lat-lon and](#)  
 727 [quasi-uniform](#) resolution grids, whether FV or SE, are similar, in general being too cloudy  
 728 over Arctic land masses. It should be emphasized that our analysis is specific to the Arc-  
 729 tic summer because of its relevance to GrIS melt rates. An improved representation of  
 730 clouds in the Arctic does not imply improved clouds at lower latitudes.

731 At the regional level, there is a halo of negative cloudiness bias around the ocean  
 732 perimeter of Greenland on all  $1 - 2^\circ$  grids, but not the VR grids. This negative cloud  
 733 bias contrasts with a positive cloud bias over the ice sheet interior. This anomaly pat-  
 734 tern is attributed to deficient orographic precipitation in the coarser model grids. With  
 735 overly smooth topography on the  $1 - 2^\circ$  grids, synoptic systems moving into Greenland  
 736 are not sufficiently lifted when encountering the steep ice margins. As a result, excess

737 precipitation falls in the GrIS interior, instead of being concentrated on the steep coastal  
 738 margins as shown by observations (Pollard & Groups, 2000; Van Kampenhout et al., 2019).  
 739 This results in a positive precipitation and cloud bias in the ice sheet interior, and a halo  
 740 of low cloud bias about the perimeter. The agreement of different observational data prod-  
 741 ucts on this bias lends confidence in the attribution of causes. The VR grids compare  
 742 better to the observations and show that orographic precipitation in Greenland is largely  
 743 resolved when the horizontal resolution is increased sufficiently.

744 We integrated the primary source and sink terms of the SMB equation over the GrIS  
 745 for each of the six grids. The [1° – 2° lat-lon and quasi-uniform](#) grids have large posi-  
 746 tive accumulation biases because they fail to resolve orographic precipitation. The quasi-  
 747 uniform SE grids have larger accumulation biases, suggesting that the FV grids are more  
 748 skillful for precipitation due to finer resolution over Greenland, and despite a polar fil-  
 749 ter. The VR grids have the most accurate accumulation rates of all the grids. The pri-  
 750 mary mass sink term of the GrIS, ice/snow melt, has similar biases; the coarse grids melt  
 751 too much, with a greater bias for quasi-uniform SE grids. In general, on coarse grids, er-  
 752 rors in the individual SMB terms are larger than the errors in the SMB itself, due to com-  
 753 pensating errors. This observation serves as a precaution; projecting mass-loss from a  
 754 glacier or ice sheet cannot be reliable if the processes representing the components of the  
 755 SMB are incorrect from the start, even if the total SMB has the right magnitude.

756 The [Arctic – GrIS](#) grid has the warmest summer lower troposphere of all grids,  
 757 yet it has less melting than the quasi-uniform resolution SE grids. This suggests that  
 758 grid resolution is somehow contributing to the melt biases in coarse grids, in a way that  
 759 is not obvious from the large-scale dynamics. We propose a mechanism: coarse grids rep-  
 760 resent ablation zones using grid cells with mixed surface types, ice-covered and ice-free.  
 761 The warmer ice-free patches may largely determine the mean state, leading to a warm  
 762 bias over the ice-covered patches of the grid cell. This mechanism is supported by anal-  
 763 ysis of melt biases binned by grid-cell ice fraction.

764 The [Arctic](#) grid substantially improves the simulated Arctic climate, including pre-  
 765 cipitation extremes and the GrIS SMB, compared to the [1°–2° lat-lon and quasi-uniform](#)  
 766 grids. The [Arctic – GrIS](#) grid has the most realistic cloud and precipitation fields, but  
 767 its summer temperatures are too warm. The 1° FV model gives a surprisingly realistic  
 768 SMB, likely due to the relatively fine resolution of Greenland on lat-lon grids (but per-  
 769 haps also because it is the most heavily tuned model configuration in CESM). In par-  
 770 ticular, a greater number of grid cells in the ablation zone reduces the influence of mixed  
 771 ice-covered/ice-free grid cells that represent ablation poorly on the other [lat-lon and quasi-](#)  
 772 uniform grids.

773 As modeling systems move away from lat-lon grids towards quasi-uniform unstruc-  
 774 tured grids, it is worth taking stock of whether this will degrade the simulated polar cli-  
 775 mate. We have found that the 1° FV model has clear advantages over the 1° SE model  
 776 for simulating the GrIS SMB. The [SE dycore is still under active development](#) (e.g., Ap-  
 777 pendix A) compared to the more mature FV dycore, and future algorithmic improve-  
 778 ments may reduce the FV-SE GrIS SMB skill gap. However, such developments are un-  
 779 likely to eliminate this skill gap entirely due to the fewer number of grid cells represent-  
 780 ing high latitude structures on quasi-uniform unstructured grids. The simulated GrIS  
 781 SMB will be adversely impacted in future CESM versions, after the FV dycore is phased  
 782 out. This finding will not interrupt the ongoing transition towards unstructured grids  
 783 in CESM, which is largely driven by gains in computational efficiency and grid refine-  
 784 ment capabilities. We therefore provide the Arctic refined-meshes to the community by  
 785 way of CESM2.2, providing users the option to simulate a more realistic GrIS SMB, al-  
 786 though at a substantial computational premium relative to conventional 1°–2° grids.

787 We are working to develop a configuration of the [Arctic](#) grid that is fully-coupled  
 788 with the CESM ocean and sea ice components and the Community Ice Sheet Model (CISM),

789 to provide multi-century projections of the state of the GrIS and its contribution to sea-  
 790 level rise. We have also developed a visualization of the **Arctic–GrIS** run, now avail-  
 791 able on youtube (see link in Acknowledgements) to increase awareness of the capabil-  
 792 ities of CESM2.2. Figure 16 shows a snapshot of this visualization, illustrating mesoscale  
 793 katabatic winds descending the southeastern slopes of the GrIS. These new grids and con-  
 794 figurations will provide new opportunities for CESM polar science, and they aim to con-  
 795 tribute to an improved understanding of the polar environment. However, we recognize  
 796 the potentially prohibitive costs for some users, and so will continue to explore differ-  
 797 ent grids, parameterizations and workflows that can provide some of the same benefits  
 798 of the VR grids, but at a lower cost.

799 **Appendix A Details on spectra-element dynamical core improvements  
 800 since the CESM2.0 release**

801 Since the CESM2.0 release of the spectral-element dynamical core documented in  
 802 Lauritzen et al. (2018) some important algorithmic improvements have been implemented  
 803 and released with CESM2.2. These pertain mainly to the flow over orography that, for  
 804 the spectral-element dynamical core, can lead to noise aligned with the element bound-  
 805 aries (Herrington et al., 2018).

806 **A1 Reference profiles**

807 Significant improvement in removing noise for flow over orography can be achieved  
 808 by using reference profiles for temperature and pressure

$$T^{(ref)} = T_0 + T_1 \Pi^{(ref)}, \quad (\text{A1})$$

$$p_s^{(ref)} = p_0 \exp\left(-\frac{\Phi_s}{R^{(d)} T_{ref}}\right), \quad (\text{A2})$$

809 (Simmons & Jiabin, 1991) where  $g$  gravity,  $T_1 = \Gamma_0 T_{ref} c_p^{(d)} / g \approx 192K$  with standard  
 810 lapse rate  $\Gamma_0 \equiv 6.5K/km$  and  $T_0 \equiv T_{ref} - T_1 \approx 97K$ ;  $T_{ref} = 288K$  ( $c_p^{(d)}$  specific heat  
 811 of dry air at constant pressure;  $R^{(d)}$  gas constant for dry air), and  $\Phi_s$  surface geopoten-  
 812 tial. The reference Exner function is

$$\Pi^{(ref)} = \left(\frac{p^{(ref)}}{p_0}\right)^\kappa \quad (\text{A3})$$

813 where  $\kappa = \frac{R^{(d)}}{c_p^{(d)}}$ . The reference surface pressure  $p_0 = 1000hPa$  and at each model level  
 814 the reference pressure  $p^{(ref)}$  is computed from  $p_s^{(ref)}$  and the standard hybrid coefficients

$$p^{(ref)}(\eta) = A(\eta)p_0 + B(\eta)p_s^{(ref)}, \quad (\text{A4})$$

815 where  $A$  and  $B$  are the standard **hybrid** coefficients (using a dry-mass generalized ver-  
 816 tical mass coordinate  $\eta$ ). These reference profiles are subtracted from the prognostic tem-  
 817 perature and pressure-level-thickness states before applying hyperviscosity:

CESM2.0 → CESM2.2

$$\nabla_\eta^4 T \rightarrow \nabla_\eta^4 (T - T^{(ref)}), \quad (\text{A5})$$

$$\nabla_\eta^4 \delta p^{(d)} \rightarrow \nabla_\eta^4 (\delta p^{(d)} - \delta p^{(ref)}). \quad (\text{A6})$$

818 This reduces spurious transport of temperature and mass up/down-slope due to the hy-  
 819 perviscosity operator.

## 820 A2 Rewriting the pressure gradient force (PGF)

821 In the CESM2.0 the following (standard) form of the pressure gradient term was  
 822 used:

$$\nabla_\eta \Phi + \frac{1}{\rho} \nabla_\eta p, \quad (A7)$$

823 where  $\Phi$  is geopotential and  $\rho = \frac{R^{(d)} T_v}{p}$  is density (for details see Lauritzen et al., 2018).  
 824 To alleviate noise for flow over orography, we switched to an Exner pressure formulation  
 825 following Taylor et al. (2020), which uses that (A7) can be written in terms of the Exner  
 826 pressure

$$\nabla_\eta \Phi + c_p^{(d)} \theta_v \nabla_\eta \Pi, \quad (A8)$$

827 where the Exner pressure is

$$\Pi \equiv \left( \frac{p}{p_0} \right)^\kappa. \quad (A9)$$

828 The derivation showing that (A7) and (A8) are equivalent is given here:

$$\begin{aligned} c_p^{(d)} \theta_v \nabla_\eta \Pi &= c_p^{(d)} \theta_v \nabla_\eta \left( \frac{p}{p_0} \right)^\kappa, \\ &= c_p^{(d)} \theta_v \kappa \left( \frac{p}{p_0} \right)^{\kappa-1} \nabla_\eta \left( \frac{p}{p_0} \right), \\ &= c_p^{(d)} \theta_v \kappa \Pi \left( \frac{p_0}{p} \right) \nabla_\eta \left( \frac{p}{p_0} \right), \\ &= \frac{c_p^{(d)} \theta_v \kappa \Pi}{p} \nabla_\eta p, \\ &= \frac{R^{(d)} \theta_v \Pi}{p} \nabla_\eta p, \\ &= \frac{R^{(d)} T_v}{p} \nabla_\eta p, \\ &= \frac{1}{\rho} \nabla_\eta p. \end{aligned}$$

829 Using the reference states from (Simmons & Jiabin, 1991),

$$\bar{T} = T_0 + T_1 \Pi, \quad (A10)$$

$$\bar{\theta} = T_0 / \Pi + T_1, \quad (A11)$$

830 we can define a geopotential as a function of Exner pressure

$$\bar{\Phi} = -c_p^{(d)} (T_0 \log \Pi + T_1 \Pi - T_1). \quad (A12)$$

831 This "balanced" geopotential obeys

$$c_p^{(d)} \bar{\theta} \nabla \Pi + \nabla \bar{\Phi} = 0 \quad (A13)$$

832 for any Exner pressure. Subtracting this "reference" profile from the PGF yields

$$\begin{aligned} \nabla_\eta \Phi + c_p^{(d)} \theta_v \nabla_\eta \Pi &= \nabla_\eta (\Phi - \bar{\Phi}) + c_p^{(d)} (\theta_v - \bar{\theta}) \nabla_\eta \Pi, \\ &= \nabla_\eta \Phi + c_p^{(d)} \theta_v \nabla_\eta \Pi + c_p^{(d)} T_0 \left[ \nabla_\eta \log \Pi - \frac{1}{\Pi} \nabla_\eta \Pi \right]. \quad (A14) \end{aligned}$$

833 In the continuum, the two formulations (left and right-hand side of (A14)) are identi-  
 834 cal. But under discretization, the second formulation can have much less truncation er-  
 835 ror.

836            **A3 Results**

837            One year averages of vertical pressure velocity at 500hPa ( `OMEGA500` ) have been  
 838            found to be a useful quantity to detect spurious up or down-drafts induced by steep orog-  
 839            raphy (Figure A1). While the true solution is not known, strong vertical velocities aligned  
 840            with element edges that are not found in the CAM-FV reference solution (Figure A1(a))  
 841            are likely not physical (spurious). The older CESM2.0 version of SE (Figure A1(d)) us-  
 842            ing the "traditional" discretization of the PGF, (A14), exhibits significant spurious noise  
 843            patters around steep orography compared to CAM-FV (e.g., around Himalayas and An-  
 844            des). This is strongly alleviated by switching to the Exner formulation of the PGF (A8;  
 845            Figure A1(c)). By also subtracting reference profiles from pressure-level thickness and  
 846            temperature, equations (A5) and (A6) respectively, reduces strong up-down drafts fur-  
 847            ther (Figure A1(d)). Switching to the CAM-SE-CSLAM version where physics ten-  
 848            dencies are computed on an quasi-equal area physics grid and using the CSLAM transport  
 849            scheme, marginal improvements are observed in terms of a smoother vertical velocity field  
 850            (Figure A1(e,f)). The configuration shown in Figure A1(d) is used for the simulations  
 851            shown in the main text of this paper.

852            It is interesting to note that the noise issues and algorithmic remedies found in the  
 853            real-world simulations discussed above, can be investigated by replacing all of physics  
 854            with a modified version of the Held-Suarez forcing (Held & Suarez, 1994). The original  
 855            formulation of the Held-Suarez idealized test case used a flat Earth ( $\Phi_s = 0$ ) and a dry  
 856            atmosphere. By simply adding the surface topography used in 'real-world' simulations  
 857            and removing the temperature relaxation in the lower part of domain ( $\sigma > 0.7$ ; see Held  
 858            and Suarez (1994) for details), surprisingly realistic vertical velocity fields (in terms of  
 859            structure) result (see Figure A2). Since this was a very useful development tool it is shared  
 860            in this manuscript.

861            **Acknowledgments**

862            This material is based upon work supported by the National Center for Atmospheric Re-  
 863            search (NCAR), which is a major facility sponsored by the NSF under Cooperative Agree-  
 864            ment 1852977. Computing and data storage resources, including the Cheyenne super-  
 865            computer (Computational and Information Systems Laboratory, 2017), were provided  
 866            by the Computational and Information Systems Laboratory (CISL) at NCAR. A. Her-  
 867            rington thanks Matt Rehme (NCAR/CISL) for his role in generating the Arctic–GrIS  
 868            visualization available on youtube ([https://www.youtube.com/watch?v=YwHgqDu75s&t=4s&ab\\_channel=NCARVisLab](https://www.youtube.com/watch?v=YwHgqDu75s&t=4s&ab_channel=NCARVisLab)).

869            The data presented in main part of this manuscript is available at <https://github.com/adamrher/2020-arcticgrids>. The source code and data for the Appendix is avail-  
 870            able at <https://github.com/PeterHjortLauritzen/CAM/tree/topo-mods>.

873            **References**

- 874            Bacmeister, J. T., Reed, K. A., Hannay, C., Lawrence, P., Bates, S., Truesdale,  
 875            J. E., ... Levy, M. (2016). Projected changes in tropical cyclone activity un-  
 876            der future warming scenarios using a high-resolution climate model. *Climatic  
 877            Change*. doi: 10.1007/s10584-016-1750-x
- 878            Bacmeister, J. T., Wehner, M. F., Neale, R. B., Gettelman, A., Hannay, C., Lau-  
 879            ritzen, P. H., ... Truesdale, J. E. (2013). Exploratory high-resolution climate  
 880            simulations using the community atmosphere model (cam). *J. Climate*, 27(9),  
 881            3073–3099. doi: 10.1175/JCLI-D-13-00387.1
- 882            Bambach, N. E., Rhoades, A. M., Hatchett, B. J., Jones, A. D., Ullrich, P. A., &  
 883            Zarzycki, C. M. (2021). Projecting climate change in south america using  
 884            variable-resolution community earth system model: An application to chile.

- 885                   *International Journal of Climatology.*
- 886 Beljaars, A., Brown, A., & Wood, N. (2004). A new parametrization of turbulent  
887 orographic form drag. *Quart. J. Roy. Meteor. Soc.*, *130*(599), 1327–1347. doi:  
888 10.1256/qj.03.73
- 889 Bogenschutz, P. A., Gettelman, A., Morrison, H., Larson, V. E., Craig, C., & Scha-  
890 nen, D. P. (2013). Higher-order turbulence closure and its impact on climate  
891 simulations in the community atmosphere model. *Journal of Climate*, *26*(23),  
892 9655–9676.
- 893 Box, J. E., Bromwich, D. H., & Bai, L.-S. (2004). Greenland ice sheet surface mass  
894 balance 1991–2000: Application of polar mm5 mesoscale model and in situ  
895 data. *Journal of Geophysical Research: Atmospheres*, *109*(D16).
- 896 Braithwaite, R. J. (1984). Calculation of degree-days for glacier-climate research.  
897 *Zeitschrift für Gletscherkunde und Glazialgeologie*, *20*(1984), 1–8.
- 898 Burakowski, E. A., Tawfik, A., Ouimette, A., Lepine, L., Zarzycki, C., Novick, K.,  
899 ... Bonan, G. (2019). Simulating surface energy fluxes using the variable-  
900 resolution community earth system model (vr-cesm). *Theoretical and Applied  
901 Climatology*, *138*(1), 115–133.
- 902 Calov, R., & Greve, R. (2005). A semi-analytical solution for the positive degree-day  
903 model with stochastic temperature variations. *Journal of Glaciology*, *51*(172),  
904 173–175.
- 905 Canuto, C., Hussaini, M. Y., Quarteroni, A., & Zang, T. (2007). *Spectral methods:  
906 Evolution to complex geometries and applications to fluid dynamics* (1st ed.).  
907 Springer.
- 908 Chang, P., Zhang, S., Danabasoglu, G., Yeager, S. G., Fu, H., Wang, H., ... oth-  
909 ers (2020). An unprecedented set of high-resolution earth system simulations  
910 for understanding multiscale interactions in climate variability and change.  
911 *Journal of Advances in Modeling Earth Systems*, *12*(12), e2020MS002298.
- 912 Chepfer, H., Bony, S., Winker, D., Cesana, G., Dufresne, J., Minnis, P., ... Zeng, S.  
913 (2010). The gcm-oriented calipso cloud product (calipso-goccp). *Journal of  
914 Geophysical Research: Atmospheres*, *115*(D4).
- 915 Collins, W. D., Rasch, P. J., Boville, B. A., Hack, J. J., McCaa, J. R., Williamson,  
916 D. L., ... Zhang, M. (2006). The formulation and atmospheric simulation  
917 of the community atmosphere model version 3 (cam3). *Journal of Climate*,  
918 *19*(11), 2144–2161.
- 919 Computational and Information Systems Laboratory. (2017). *Cheyenne: HPE/SGI  
920 ICE XA System (Climate Simulation Laboratory)*, Boulder, CO: National  
921 Center for Atmospheric Research. doi: 10.5065/D6RX99HX
- 922 Copernicus, C. (2019). Era5 monthly averaged data on pressure levels from  
923 1979 to present. URL: <https://cds.climate.copernicus.eu>. doi: 10.24381/  
924 cds.6860a573
- 925 Craig, C., Bacmeister, J., Callaghan, P., Eaton, B., Gettelman, A., Goldhaber, S. N.,  
926 ... Vitt, F. M. (2021). *Cam6.3 user's guide* (Tech. Rep.). NCAR/TN-  
927 571+EDD. doi: 10.5065/Z953-ZC95
- 928 Danabasoglu, G., Lamarque, J.-F., Bacmeister, J., Bailey, D., DuVivier, A., Ed-  
929 wards, J., ... others (2020). The community earth system model ver-  
930 sion 2 (cesm2). *Journal of Advances in Modeling Earth Systems*, *12*(2),  
931 e2019MS001916.
- 932 Danielson, J., & Gesch, D. (2011). *Global multi-resolution terrain elevation data  
933 2010 (GMTED2010)* (Open-File Report 2011-1073). U.S. Geological Survey.  
934 (<http://pubs.usgs.gov/of/2011/1073/pdf/of2011-1073.pdf>)
- 935 Danielson, J. J., & Gesch, D. B. (2011). *Global multi-resolution terrain elevation  
936 data 2010 (GMTED2010)* (Open File Rep. No. 2011-1073). US Geological Sur-  
937 vey. doi: <https://doi.org/10.3133/ofr20111073>
- 938 Dennis, J., Edwards, J., Evans, K. J., Gilba, O., Lauritzen, P. H., Mirin, A. A., ...  
939 Worley, P. H. (2012). CAM-SE: A scalable spectral element dynamical core for

- the Community Atmosphere Model. *Int. J. High. Perform. C.*, *26*(1), 74–89. Retrieved from <http://hpc.sagepub.com/content/26/1/74.abstract> doi: 10.1177/1094342011428142
- Dennis, J., Fournier, A., Spotz, W., St-Cyr, A., Taylor, M., Thomas, S., & Tufo, H. (2005). High-resolution mesh convergence properties and parallel efficiency of a spectral element atmospheric dynamical core. *ijhpc*, *19*, 225–235. doi: 10.1177/1094342005056108
- Evans, K. J., Kennedy, J. H., Lu, D., Forrester, M. M., Price, S., Fyke, J., ... others (2019). Livvkit 2.1: automated and extensible ice sheet model validation. *Geoscientific Model Development*, *12*(3), 1067–1086.
- Eyring, V., Bony, S., Meehl, G. A., Senior, C. A., Stevens, B., Stouffer, R. J., & Taylor, K. E. (2016). Overview of the coupled model intercomparison project phase 6 (cmip6) experimental design and organization. *Geoscientific Model Development*, *9*(5), 1937–1958.
- Fettweis, X., Franco, B., Tedesco, M., Van Angelen, J., Lenaerts, J. T., van den Broeke, M. R., & Gallée, H. (2013). Estimating the greenland ice sheet surface mass balance contribution to future sea level rise using the regional atmospheric climate model mar. *The Cryosphere*, *7*(2), 469–489.
- Gettelman, A., Callaghan, P., Larson, V., Zarzycki, C., Bacmeister, J., Lauritzen, P., ... Neale, R. (2017). Regional climate simulations with the community earth system model. *J. Adv. Model. Earth Syst.*. (submitted)
- Gettelman, A., Hannay, C., Bacmeister, J. T., Neale, R. B., Pendergrass, A., Danabasoglu, G., ... others (2019). High climate sensitivity in the community earth system model version 2 (cesm2). *Geophysical Research Letters*, *46*(14), 8329–8337.
- Gettelman, A., & Morrison, H. (2015). Advanced two-moment bulk microphysics for global models. part i: Off-line tests and comparison with other schemes. *Journal of Climate*, *28*(3), 1268–1287.
- Gettelman, A., Morrison, H., Santos, S., Bogsenschutz, P., & Caldwell, P. (2015). Advanced two-moment bulk microphysics for global models. part ii: Global model solutions and aerosol–cloud interactions. *Journal of Climate*, *28*(3), 1288–1307.
- Golaz, J.-C., Larson, V. E., & Cotton, W. R. (2002). A pdf-based model for boundary layer clouds. part i: Method and model description. *Journal of the Atmospheric Sciences*, *59*(24), 3540–3551. doi: 10.1175/1520-0469(2002)059<3540:apbmfb>2.0.co;2
- Guba, O., Taylor, M. A., Ullrich, P. A., Overfelt, J. R., & Levy, M. N. (2014). The spectral element method (sem) on variable-resolution grids: evaluating grid sensitivity and resolution-aware numerical viscosity. *Geosci. Model Dev.*, *7*(6), 2803–2816. doi: 10.5194/gmd-7-2803-2014
- Guo, Z., Wang, M., Qian, Y., Larson, V. E., Ghan, S., Ovchinnikov, M., ... Zhou, T. (2015). Parametric behaviors of clubb in simulations of low clouds in the community atmosphere model (cam). *Journal of Advances in Modeling Earth Systems*, *7*(3), 1005–1025.
- Hansen, N., Simonsen, S. B., Boberg, F., Kittel, C., Orr, A., Souverijns, N., ... Mottram, R. (2022). Brief communication: Impact of common ice mask in surface mass balance estimates over the antarctic ice sheet. *The Cryosphere*, *16*(2), 711–718.
- Held, I. M., & Suarez, M. J. (1994). A proposal for the intercomparison of the dynamical cores of atmospheric general circulation models. *Bull. Am. Meteorol. Soc.*, *75*, 1825–1830.
- Herrington, A. R., Lauritzen, P., Taylor, M. A., Goldhaber, S., Eaton, B. E., Bacmeister, J., ... Ullrich, P. (2018). Physics-dynamics coupling with element-based high-order galerkin methods: quasi equal-area physics grid. *Mon. Wea. Rev.*, *147*, 69–84. doi: 10.1175/MWR-D-18-0136.1

- 995 Herrington, A. R., Lauritzen, P. H., Reed, K. A., Goldhaber, S., & Eaton, B. E.  
 996 (2019). Exploring a lower resolution physics grid in cam-se-cslam. *Journal of*  
 997 *Advances in Modeling Earth Systems*, 11.
- 998 Herrington, A. R., & Reed, K. A. (2018). An idealized test of the response of the  
 999 community atmosphere model to near-grid-scale forcing across hydrostatic  
 1000 resolutions. *J. Adv. Model. Earth Syst.*, 10(2), 560–575.
- 1001 Herrington, A. R., & Reed, K. A. (2020). On resolution sensitivity in the commu-  
 1002 nity atmosphere model. *Quarterly Journal of the Royal Meteorological Society*,  
 1003 146(733), 3789–3807.
- 1004 Hurrell, J. W., Hack, J. J., Shea, D., Caron, J. M., & Rosinski, J. (2008). A new  
 1005 sea surface temperature and sea ice boundary dataset for the community at-  
 1006 mosphere model. *Journal of Climate*, 21(19), 5145–5153.
- 1007 Jablonowski, C., & Williamson, D. L. (2011). The pros and cons of diffusion, fil-  
 1008 ters and fixers in atmospheric general circulation models. In P. H. Lauritzen,  
 1009 C. Jablonowski, M. Taylor, & R. Nair (Eds.), *Numerical techniques for global*  
 1010 *atmospheric models* (pp. 381–493). Berlin, Heidelberg: Springer Berlin Heidel-  
 1011 berg. doi: 10.1007/978-3-642-11640-7\_13
- 1012 Lauritzen, P. H., Bacmeister, J. T., Callaghan, P. F., & Taylor, M. A. (2015).  
 1013 NCAR\_Topo (v1.0): NCAR global model topography generation soft-  
 1014 ware for unstructured grids. *Geosci. Model Dev.*, 8(12), 3975–3986. doi:  
 1015 10.5194/gmd-8-3975-2015
- 1016 Lauritzen, P. H., Jablonowski, C., Taylor, M., & Nair, R. D. (2010). Rotated  
 1017 versions of the jablonowski steady-state and baroclinic wave test cases: A  
 1018 dynamical core intercomparison. *J. Adv. Model. Earth Syst.*, 2(15), 34 pp.
- 1019 Lauritzen, P. H., Mirin, A., Truesdale, J., Raeder, K., Anderson, J., Bacmeister, J.,  
 1020 & Neale, R. B. (2011). Implementation of new diffusion/filtering operators  
 1021 in the CAM-FV dynamical core. *Int. J. High Perform. Comput. Appl.*. doi:  
 1022 10.1177/1094342011410088
- 1023 Lauritzen, P. H., Nair, R., Herrington, A., Callaghan, P., Goldhaber, S., Dennis, J.,  
 1024 ... Dubos, T. (2018). NCAR release of CAM-SE in CESM2.0: A reformula-  
 1025 tion of the spectral-element dynamical core in dry-mass vertical coordinates  
 1026 with comprehensive treatment of condensates and energy. *J. Adv. Model.*  
 1027 *Earth Syst.*, 10(7), 1537–1570. doi: 10.1029/2017MS001257
- 1028 Lauritzen, P. H., Taylor, M. A., Overfelt, J., Ullrich, P. A., Nair, R. D., Goldhaber,  
 1029 & Kelly, R. (2017). CAM-SE-CSLAM: Consistent coupling of a conser-  
 1030 vative semi-lagrangian finite-volume method with spectral element dynamics.  
 1031 *Mon. Wea. Rev.*, 145(3), 833–855. doi: 10.1175/MWR-D-16-0258.1
- 1032 Lawrence, D. M., Fisher, R. A., Koven, C. D., Oleson, K. W., Swenson, S. C., Bo-  
 1033 nan, G., ... others (2019). The community land model version 5: Description  
 1034 of new features, benchmarking, and impact of forcing uncertainty. *Journal of*  
 1035 *Advances in Modeling Earth Systems*, 11(12), 4245–4287.
- 1036 Lin, S.-J. (2004). A 'vertically Lagrangian' finite-volume dynamical core for global  
 1037 models. *Mon. Wea. Rev.*, 132, 2293–2307.
- 1038 Lin, S.-J., & Rood, R. B. (1997). An explicit flux-form semi-Lagrangian shallow-  
 1039 water model on the sphere. *Q.J.R.Meteorol.Soc.*, 123, 2477–2498.
- 1040 Lipscomb, W. H., Fyke, J. G., Vizcaíno, M., Sacks, W. J., Wolfe, J., Vertenstein,  
 1041 M., ... Lawrence, D. M. (2013). Implementation and initial evaluation of the  
 1042 glimmer community ice sheet model in the community earth system model.  
 1043 *Journal of Climate*, 26(19), 7352–7371.
- 1044 Loeb, N. G., Doelling, D. R., Wang, H., Su, W., Nguyen, C., Corbett, J. G., ...  
 1045 Kato, S. (2018). Clouds and the earth's radiant energy system (ceres) energy  
 1046 balanced and filled (ebaf) top-of-atmosphere (toa) edition-4.0 data product.  
 1047 *Journal of Climate*, 31(2), 895–918.
- 1048 Lofverstrom, M., Fyke, J. G., Thayer-Calder, K., Muntjewerf, L., Vizcaino, M.,  
 1049 Sacks, W. J., ... Bradley, S. L. (2020). An efficient ice sheet/earth sys-

- tem model spin-up procedure for cesm2-cism2: Description, evaluation, and broader applicability. *Journal of Advances in Modeling Earth Systems*, 12(8), e2019MS001984.
- Morlighem, M., Rignot, E., Mouginot, J., Seroussi, H., & Larour, E. (2014). Deeply incised submarine glacial valleys beneath the greenland ice sheet. *Nature Geoscience*, 7(6), 418–422.
- Mottram, R., Boberg, F., Langen, P., Yang, S., Rodehacke, C., Christensen, J. H., & Madsen, M. S. (2017). Surface mass balance of the greenland ice sheet in the regional climate model hirham5: Present state and future prospects. *Low Temp. Sci.*, 75, 105–115.
- Muntjewerf, L., Sacks, W. J., Lofverstrom, M., Fyke, J., Lipscomb, W. H., Ernani da Silva, C., ... Sellevold, R. (2021). Description and Demonstration of the Coupled Community Earth System Model v2–Community Ice Sheet Model v2 (CESM2-CISM2). *Journal of Advances in Modeling Earth Systems*, 13(6), e2020MS002356.
- Neale, R. B., Richter, J. H., & Jochum, M. (2008). The impact of convection on ENSO: From a delayed oscillator to a series of events. *J. Climate*, 21, 5904–5924.
- Noël, B., Van De Berg, W., Van Meijgaard, E., Kuipers Munneke, P., Van De Wal, R., & Van Den Broeke, M. (2015). Evaluation of the updated regional climate model racmo2. 3: summer snowfall impact on the greenland ice sheet. *The Cryosphere*, 9(5), 1831–1844.
- Noël, B., van de Berg, W. J., Lhermitte, S., & van den Broeke, M. R. (2019). Rapid ablation zone expansion amplifies north greenland mass loss. *Science advances*, 5(9), eaaw0123.
- Noël, B., van de Berg, W. J., Van Wessem, J. M., Van Meijgaard, E., Van As, D., Lenaerts, J., ... others (2018). Modelling the climate and surface mass balance of polar ice sheets using racmo2–part 1: Greenland (1958–2016). *The Cryosphere*, 12(3), 811–831.
- Obrien, T. A., Collins, W. D., Kashinath, K., Rübel, O., Byna, S., Gu, J., ... Ullrich, P. A. (2016). Resolution dependence of precipitation statistical fidelity in hindcast simulations. *J. Adv. Model. Earth Syst.*, 8(2), 976–990. Retrieved from <http://dx.doi.org/10.1002/2016ms000671> doi: 10.1002/2016ms000671
- Ohmura, A. (2001). Physical basis for the temperature-based melt-index method. *Journal of applied Meteorology*, 40(4), 753–761.
- Pfister, G. G., Eastham, S. D., Arellano, A. F., Aumont, B., Barsanti, K. C., Barth, M. C., ... others (2020). The multi-scale infrastructure for chemistry and aerosols (musica). *Bulletin of the American Meteorological Society*, 101(10), E1743–E1760.
- Pollard, D. (2010). A retrospective look at coupled ice sheet–climate modeling. *Climatic Change*, 100(1), 173–194.
- Pollard, D., & Groups, P. P. (2000). Comparisons of ice-sheet surface mass budgets from paleoclimate modeling intercomparison project (pmip) simulations. *Global and Planetary Change*, 24(2), 79–106.
- Pope, V., & Stratton, R. (2002). The processes governing horizontal resolution sensitivity in a climate model. *Climate Dynamics*, 19(3-4), 211–236.
- Putman, W. M., & Lin, S.-J. (2007). Finite-volume transport on various cubed-sphere grids. *J. Comput. Phys.*, 227(1), 55–78.
- Rae, J., Adalgeirsdóttir, G., Edwards, T. L., Fettweis, X., Gregory, J., Hewitt, H., ... others (2012). Greenland ice sheet surface mass balance: evaluating simulations and making projections with regional climate models. *The Cryosphere*, 6(6), 1275–1294.
- Rasch, P. J., & Williamson, D. L. (1990). Computational aspects of moisture transport in global models of the atmosphere. *Q. J. R. Meteorol. Soc.*, 116, 1071–

- 1090.
- 1105 Reeh, N. (1991). Parameterization of melt rate and surface temperature in the  
1106 greenland ice sheet. *Polarforschung*, 59(3), 113–128.
- 1108 Rhoades, A. M., Huang, X., Ullrich, P. A., & Zarzycki, C. M. (2016). Characterizing  
1109 sierra nevada snowpack using variable-resolution cesm. *Journal of Applied Me-*  
1110 *teorology and Climatology*, 55(1), 173-196. Retrieved from <https://doi.org/10.1175/JAMC-D-15-0156.1> doi: 10.1175/JAMC-D-15-0156.1
- 1112 Richter, J. H., Sassi, F., & Garcia, R. R. (2010). Toward a physically based gravity  
1113 wave source parameterization in a general circulation model. *J. Atmos. Sci.*,  
1114 67, 136-156. doi: dx.doi.org/10.1175/2009JAS3112.1
- 1115 Rignot, E., & Mouginot, J. (2012). Ice flow in greenland for the international polar  
1116 year 2008–2009. *Geophysical Research Letters*, 39(11).
- 1117 Roeckner, E., Brokopf, R., Esch, M., Giorgetta, M., Hagemann, S., Kornblueh, L.,  
1118 ... Schulzweida, U. (2006). Sensitivity of simulated climate to horizontal  
1119 and vertical resolution in the echam5 atmosphere model. *Journal of Climate*,  
1120 19(16), 3771–3791.
- 1121 Sellevold, R., Van Kampenhout, L., Lenaerts, J., Noël, B., Lipscomb, W. H., &  
1122 Vizcaino, M. (2019). Surface mass balance downscaling through elevation  
1123 classes in an earth system model: Application to the greenland ice sheet. *The*  
1124 *Cryosphere*, 13(12), 3193–3208.
- 1125 Serreze, M. C., Barrett, A. P., Slater, A. G., Steele, M., Zhang, J., & Trenberth,  
1126 K. E. (2007). The large-scale energy budget of the arctic. *Journal of Geophysi-*  
1127 *cal Research: Atmospheres*, 112(D11).
- 1128 Simmons, A. J., & Jiabin, C. (1991). The calculation of geopotential and  
1129 the pressure gradient in the ECMWF atmospheric model: Influence on  
1130 the simulation of the polar atmosphere and on temperature analyses.  
1131 *Quart. J. Roy. Meteor. Soc.*, 117(497), 29-58. Retrieved from <https://rmetsonlinelibrary.wiley.com/doi/abs/10.1002/qj.49711749703> doi:  
1132 <https://doi.org/10.1002/qj.49711749703>
- 1134 Small, R. J., Bacmeister, J., Bailey, D., Baker, A., Bishop, S., Bryan, F., ... Verten-  
1135 stein, M. (2014). A new synoptic scale resolving global climate simulation  
1136 using the community earth system model. *J. Adv. Model. Earth Syst.*, 6(4),  
1137 1065–1094. doi: 10.1002/2014MS000363
- 1138 Suarez, M. J., & Takacs, L. L. (1995). Volume 5 documentation of the aries/geos dy-  
1139 namical core: Version 2.
- 1140 Taylor, M. A., & Fournier, A. (2010). A compatible and conservative spectral el-  
1141 ement method on unstructured grids. *J. Comput. Phys.*, 229(17), 5879 - 5895.  
1142 doi: 10.1016/j.jcp.2010.04.008
- 1143 Taylor, M. A., Guba, O., Steyer, A., Ullrich, P. A., Hall, D. M., & Eldred, C.  
1144 (2020). An energy consistent discretization of the nonhydrostatic equations  
1145 in primitive variables. *Journal of Advances in Modeling Earth Systems*, 12(1).  
1146 doi: 10.1029/2019MS001783
- 1147 Taylor, M. A., Tribbia, J., & Iskandarani, M. (1997). The spectral element method  
1148 for the shallow water equations on the sphere. *J. Comput. Phys.*, 130, 92-108.
- 1149 Team, E. J. S., Balaji, V., Boville, B., Collins, N., Craig, T., Cruz, C., ... others  
1150 (2021). *Esmf user guide* (Tech. Rep.).
- 1151 Ullrich, P. A., & Taylor, M. A. (2015). Arbitrary-order conservative and consis-  
1152 tent remapping and a theory of linear maps: Part i. *Monthly Weather Review*,  
1153 143(6), 2419–2440.
- 1154 Ullrich, P. A., Zarzycki, C. M., McClenny, E. E., Pinheiro, M. C., Stansfield, A. M.,  
1155 & Reed, K. A. (2021). Tempestextremes v2. 1: a community framework for  
1156 feature detection, tracking and analysis in large datasets. *Geoscientific Model*  
1157 *Development Discussions*, 1–37.
- 1158 Van Angelen, J., Lenaerts, J., Lhermitte, S., Fettweis, X., Kuipers Munneke, P.,  
1159 Van den Broeke, M., ... Smeets, C. (2012). Sensitivity of greenland ice

- sheet surface mass balance to surface albedo parameterization: a study with a  
regional climate model. *The Cryosphere*, 6(5), 1175–1186.
- van Kampenhout, L., Lenaerts, J. T., Lipscomb, W. H., Lhermitte, S., Noël, B.,  
Vizcaíno, M., ... van den Broeke, M. R. (2020). Present-day greenland ice  
sheet climate and surface mass balance in cesm2. *Journal of Geophysical  
Research: Earth Surface*, 125(2).
- Van Kampenhout, L., Rhoades, A. M., Herrington, A. R., Zarzycki, C. M., Lenaerts,  
J., Sacks, W. J., & Van Den Broeke, M. R. (2019). Regional grid refinement  
in an earth system model: impacts on the simulated greenland surface mass  
balance. *The Cryosphere*, 13(6), 1547–1564.
- Wan, H., Giorgetta, M. A., Zängl, G., Restelli, M., Majewski, D., Bonaventura, L.,  
... others (2013). "the icon-1.2 hydrostatic atmospheric dynamical core on  
triangular grids, part i: formulation and performance of the baseline version".  
*Geosci. Model Dev.*, 6, 735–763.
- Williamson, D. (2007). The evolution of dynamical cores for global atmospheric  
models. *J. Meteor. Soc. Japan*, 85, 241–269.
- Williamson, D. (2008). Convergence of aqua-planet simulations with increasing res-  
olution in the community atmospheric model, version 3. *Tellus A*, 60(5), 848–  
862. doi: 10.1111/j.1600-0870.2008.00339.x
- Zarzycki, C. M., Jablonowski, C., & Taylor, M. A. (2014). Using variable-resolution  
meshes to model tropical cyclones in the community atmosphere model. *Mon.  
Wea. Rev.*, 142(3), 1221–1239. doi: 10.1175/MWR-D-13-00179.1
- Zhang, G., & McFarlane, N. (1995). Sensitivity of climate simulations to the  
parameterization of cumulus convection in the canadian climate center general-  
circulation model. *ATMOSPHERE-OCEAN*, 33(3), 407–446.

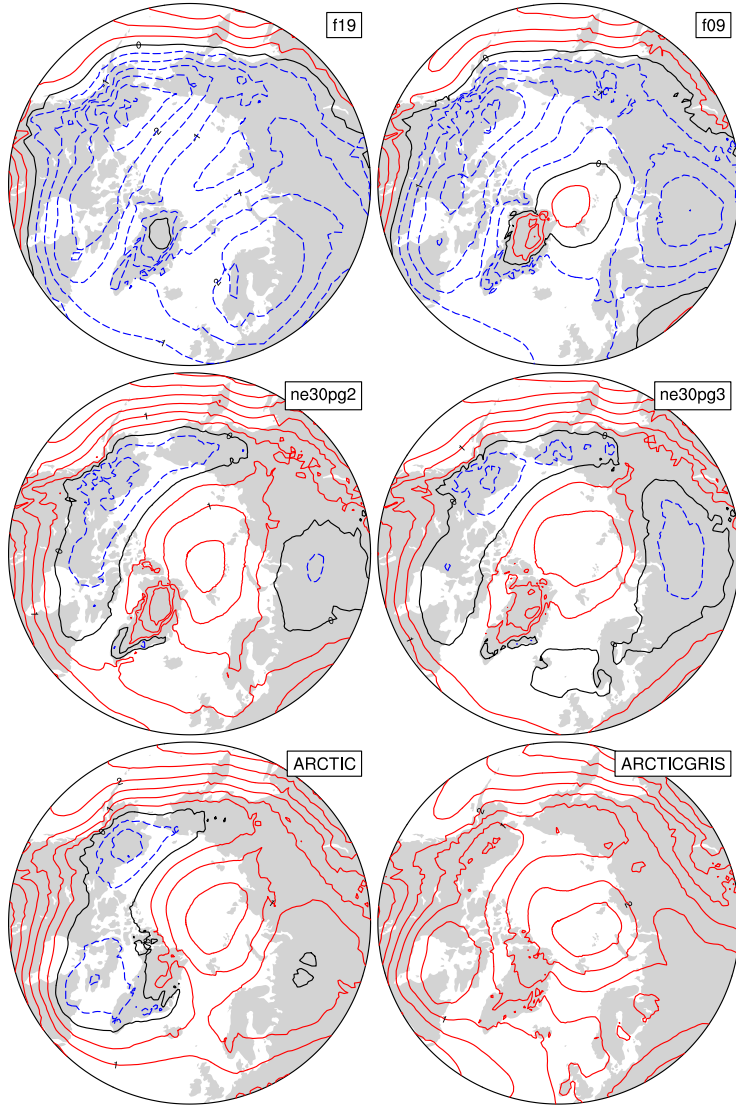


**Figure 6.** 1979-1998 lower troposphere, northern hemisphere summer virtual temperature biases, computed as the difference from ERA5. Lower troposphere layer mean virtual temperature is derived from the 1000 hPa - 500h Pa geopotential thickness, using the hypsometric equation. Differences are computed after mapping the ERA5 data to the finite-volume grids since the geopotential field is only available on the output tapes in the spectral-element runs that have been interpolated to the f09 grid, inline.

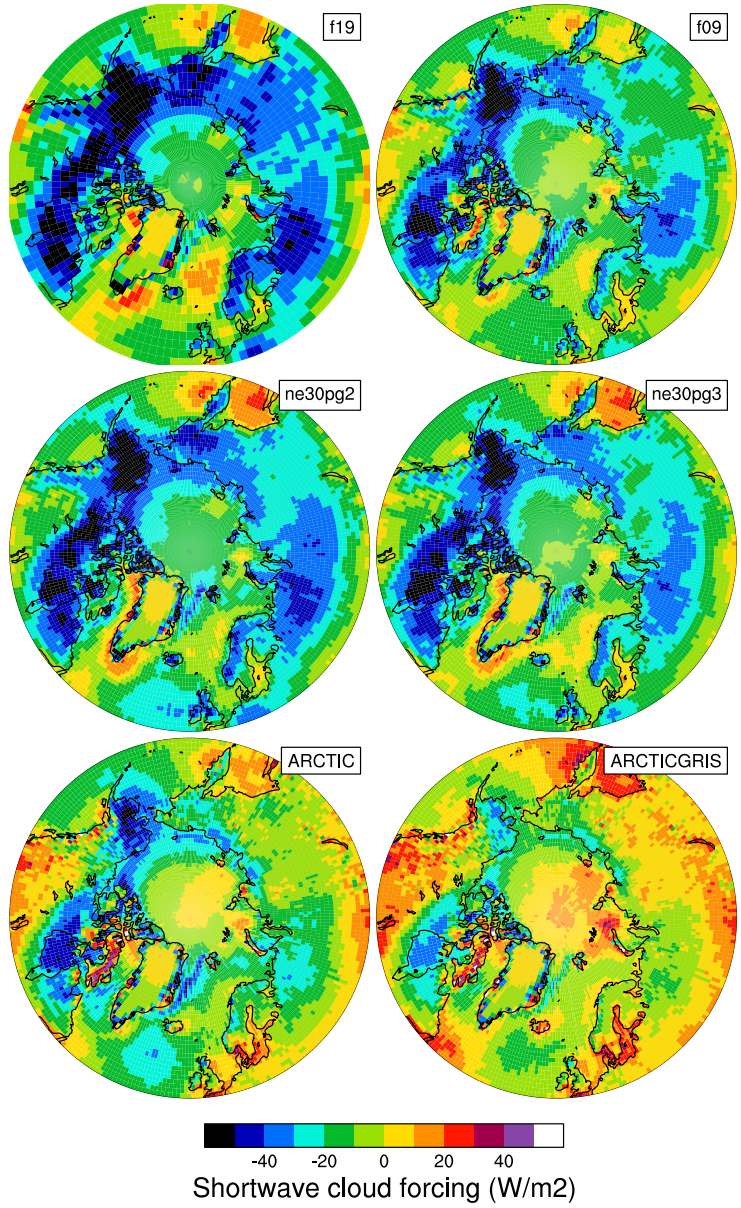


**Figure 7.** 1979-1998 Northern Hemisphere summer shortwave cloud forcing bias, relative to the CERES-EBAF gridded dataset. Shortwave cloud forcing is defined as the difference between all-sky and clear-sky net shortwave fluxes at the top of the atmosphere. Differences are computed after mapping all model output to the 1° CERES-EBAF grid.

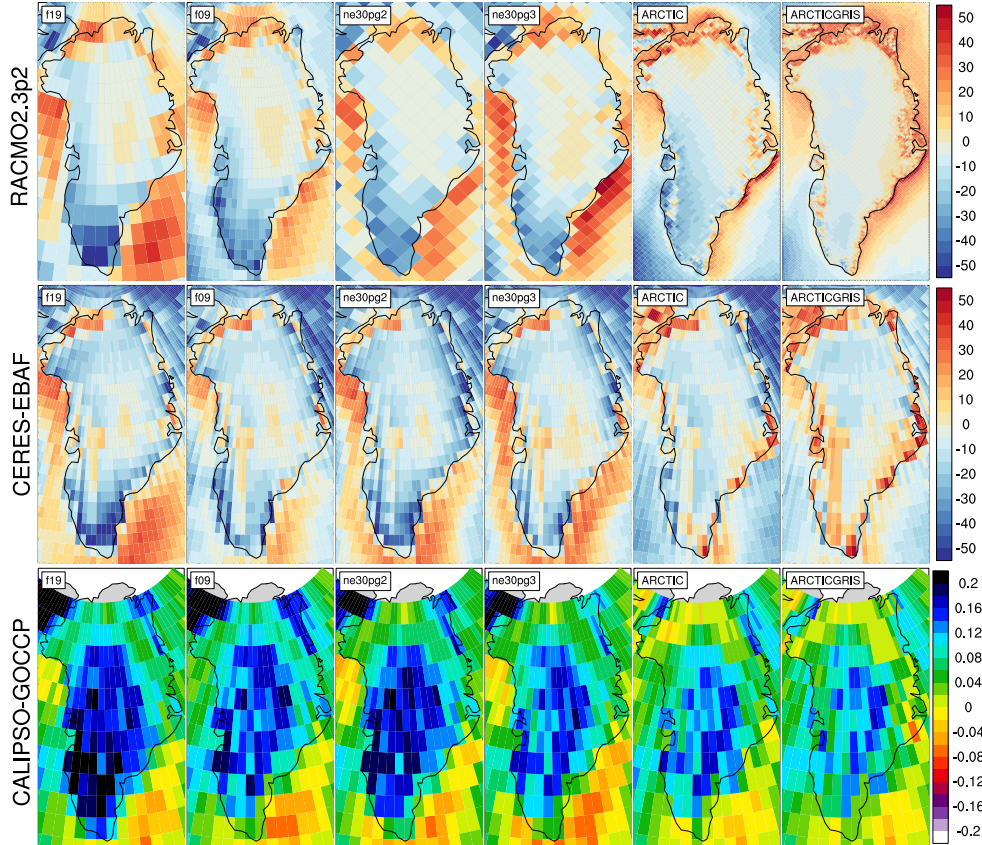


**Figure 8.** 1979-1998 northern hemisphere summer surface incident shortwave radiation bias ( $\text{W}/\text{m}^2$ ), computed as the difference (top) from RACMO2.3p2, and (middle) the CERES-EBAF dataset, and the (bottom) total cloud fraction bias relative to the CALIPSO dataset. CALIPSO and CERES differences are found by mapping the model output to the  $1^\circ$  grid, and differences in the bottom panel are computed after mapping the RACMO2.3p2 dataset to the individual model grids. Note that the averaging period for the CALIPSO-GOCCP and CERES-EBAF panels, 2006-2017 and 2003-2020, respectively, are different from the averaging period for the model results.

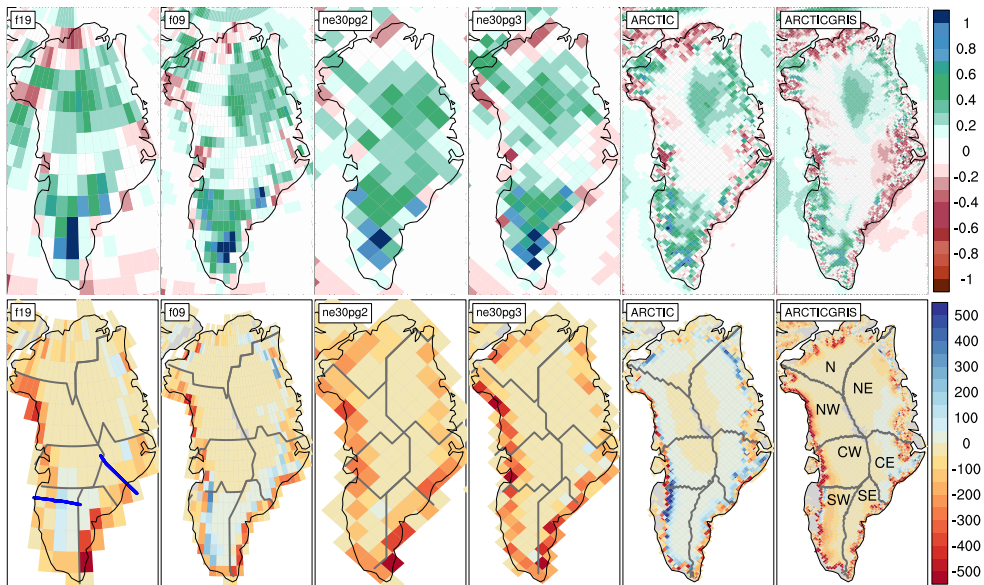


**Figure 9.** 1979-1998 (top) annual precipitation and (bottom) ice/snow melt biases relative to RACMO2.3p2, evaluated on the native model grids. The precipitation biases are expressed as fractional changes, whereas the melt biases are absolute changes (mm/yr). In the bottom panel, the Rignot and Mouginot (2012) basin boundaries are shown in grey for each model grid. Note that Figure 11 uses the basin boundaries for the two common ice masks, shown in the f19 and ne30pg2 panels, in computing the basin-scale integrals. Blue lines in the f19 panel show the location of the two transects plotted in Figure 12.

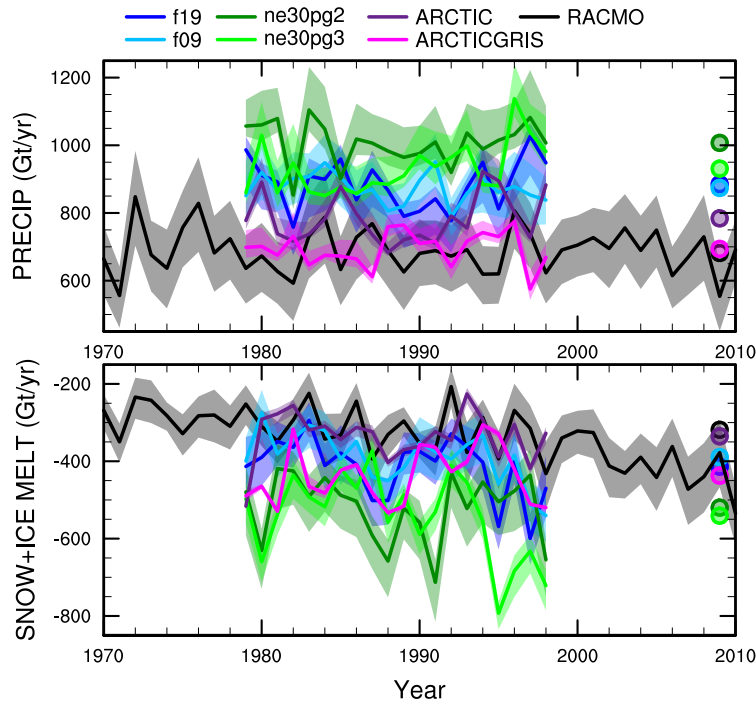


**Figure 10.** Time-series of annual (solid+liquid) precipitation (top) and annual runoff (bottom) integrated over the Greenland Ice Sheet for all six simulations and compared to the RACMO datasets. The time-series were generated using the common ice mask approach, which results in up to 4 ensembles, with the mean value given by the solid line and shading spanning the extent of the ensemble members.

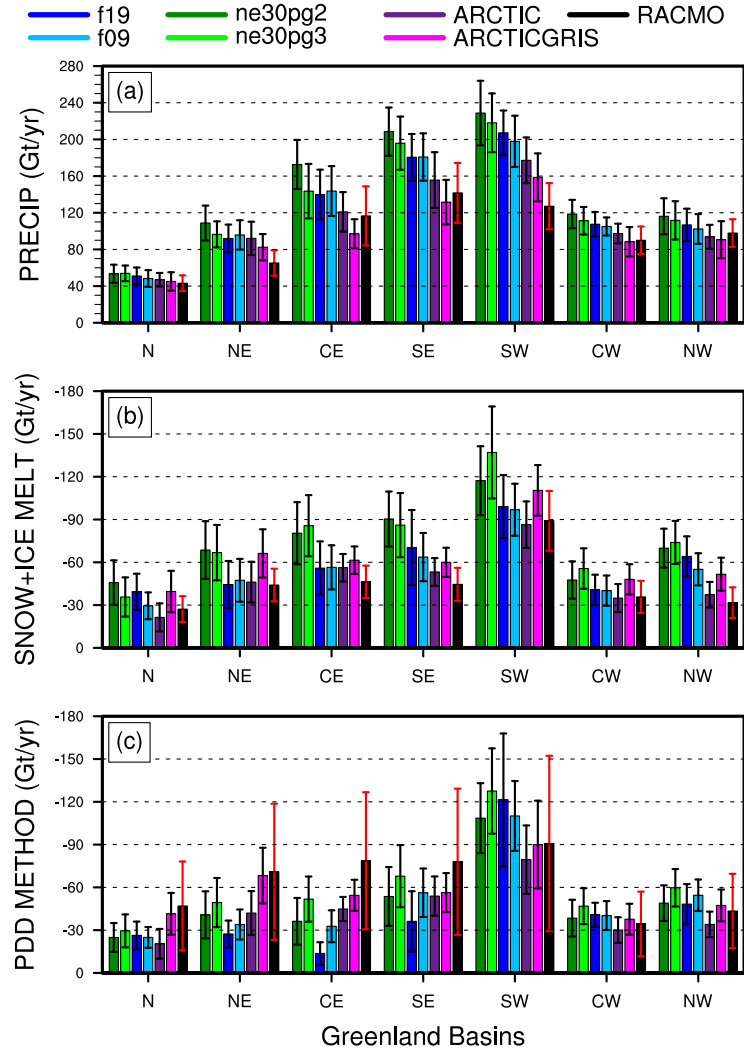


**Figure 11.** 1979–1998 basin integrated components of the SMB; (top) precipitation, (middle) ice/snow melt and (bottom) ice/snow melt estimated from the PDD method. Whiskers span the max/min of the four ensemble members generated from the common-ice-mask approach. Basin definitions are after Rignot and Mouginot (2012), and are found on the common ice masks using a nearest neighbor approach, and shown in Figure 9.

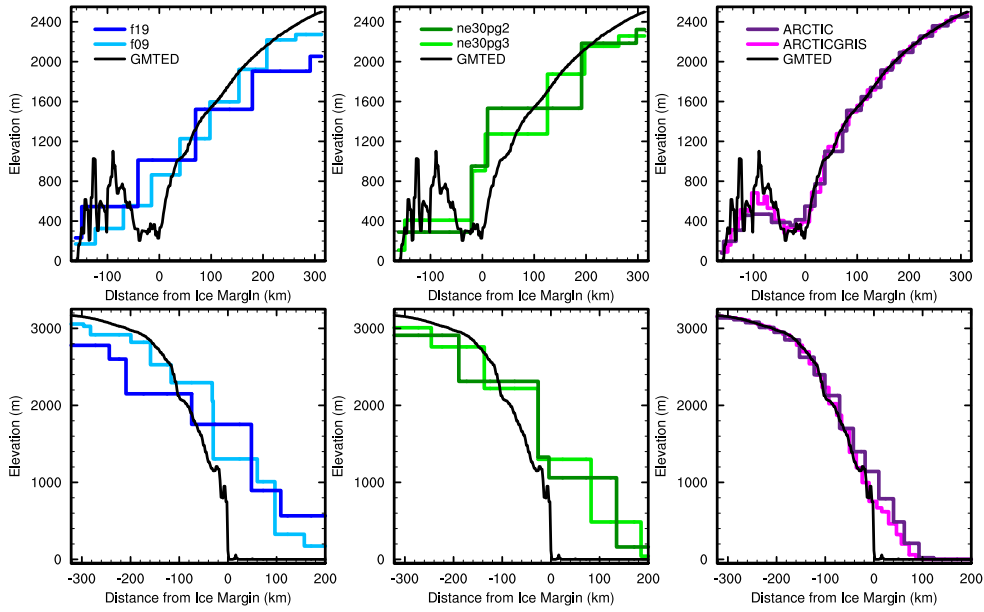


**Figure 12.** Model surface elevation along the (top) K-transect, and (bottom) a transect spanning the central dome down to the Kangerlussuaq glacier in southeast Greenland, for all model grids. The GMTED reference surface is a 1 km surface elevation dataset (J. Danielson & Gesch, 2011) used for generating the CAM topographic boundary conditions.

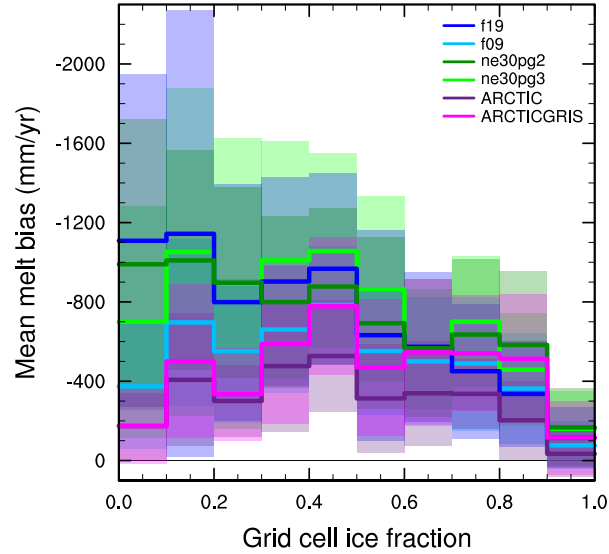


**Figure 13.** Fractional melt bias over the GrIS, computed relative to the RACMO datasets using the common ice mask approach, and conditionally sampled by grid cell ice fraction provided by the common ice masks. Solid lines are the mean of the distribution with  $\pm$  one standard deviation expressed by shading.

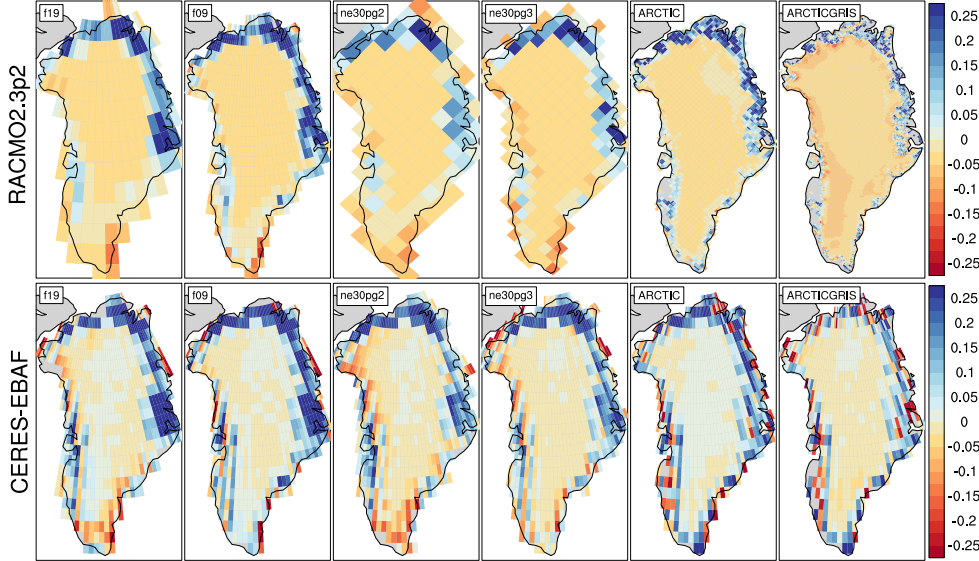


**Figure 14.** 1979-1998 northern hemisphere summer albedo bias (fraction), computed as the difference (top) from RACMO2.3p2, and (bottom) CERES-EBAF dataset. RACMO2.3p2 differences are found by mapping the model output to the individual model grids, and differences in the bottom panel are computed after mapping the individual model grids to the CERES-EBAF  $1^{\circ}$  grid. Note that the averaging period for CERES-EBAF panels are 2003-2020, which is different from the averaging period for the model results.

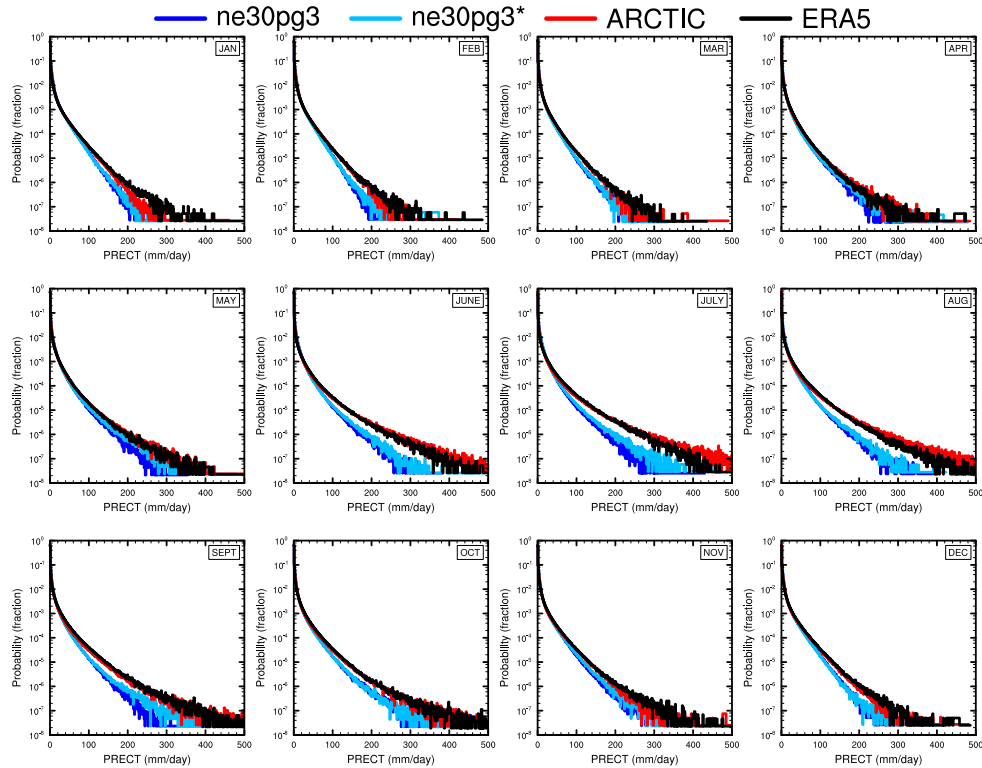


**Figure 15.** PDFs of the total precipitation rate associated with tracked storms, by month, in the ne30pg3, ne30pg3\* and Arctic runs, and compared with the ERA5 dataset.

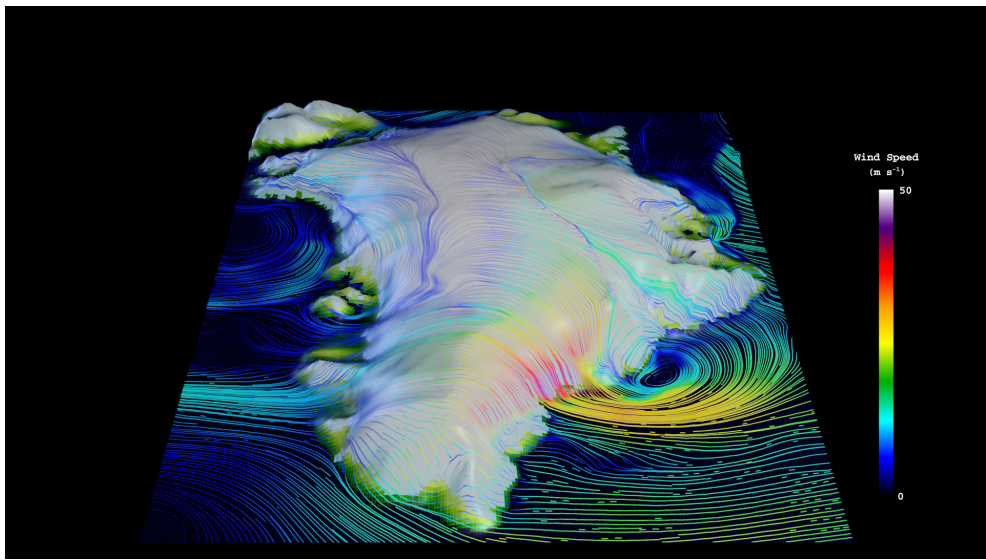


**Figure 16.** Snapshot of the lowest model level streamlines from the `Arctic - GrIS` visualization, with color shading denoting the wind magnitude.

## OMEGA500, 1 year average, F2000climo, 32 levels

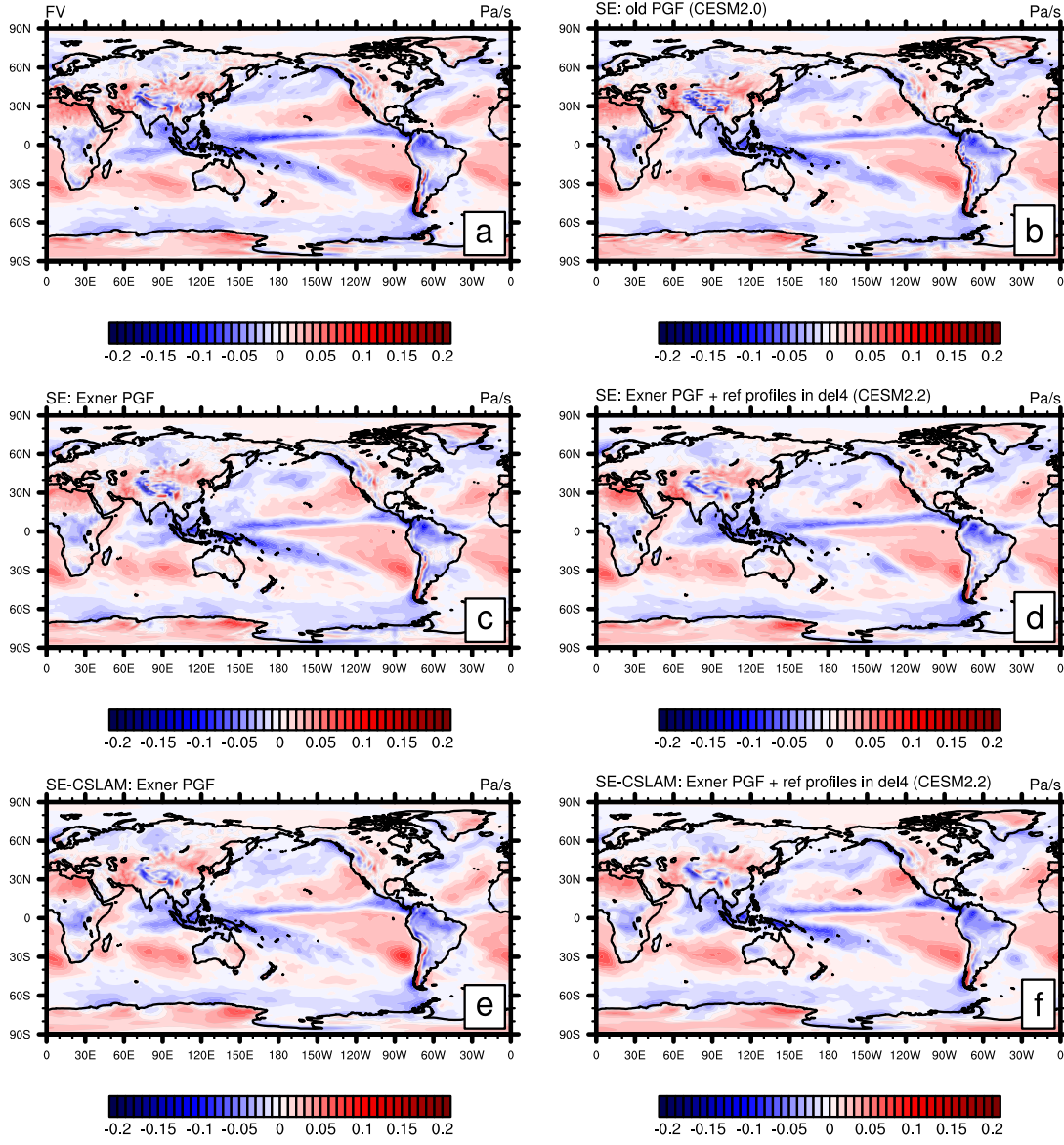


**Figure A1.** One year averages of vertical pressure velocity at 500hPa (OMEGA500) using (a) CAM-FV (Finite-Volume dynamical core) and (b-f) various versions of the spectral-element (SE) dynamical core at approximately 1° horizontal resolution and using 32 levels. (b) is equivalent to the CESM2.0 version of the SE dynamical core using the "traditional"/"old" discretization of the pressure-gradient force (PGF). Plot (c) is equivalent to configuration (b) but using the Exner form of the PGF. Plot (d) is the same as configuration (c) but also subtracting reference profiles from pressure and temperature before applying hyperviscosity operators (which is equivalent to the CESM2.2 version of SE in terms of the dynamical core). Plots (e) and (f) are equivalent to (c) and (d), respectively, by using the SE-CSLAM (ne30pg3) version of the SE dynamical core (i.e. separate quasi-uniform physics grid and CSLAM transport scheme).

OMEGA500, 18 months average, FHS94 forcing, 32 levels

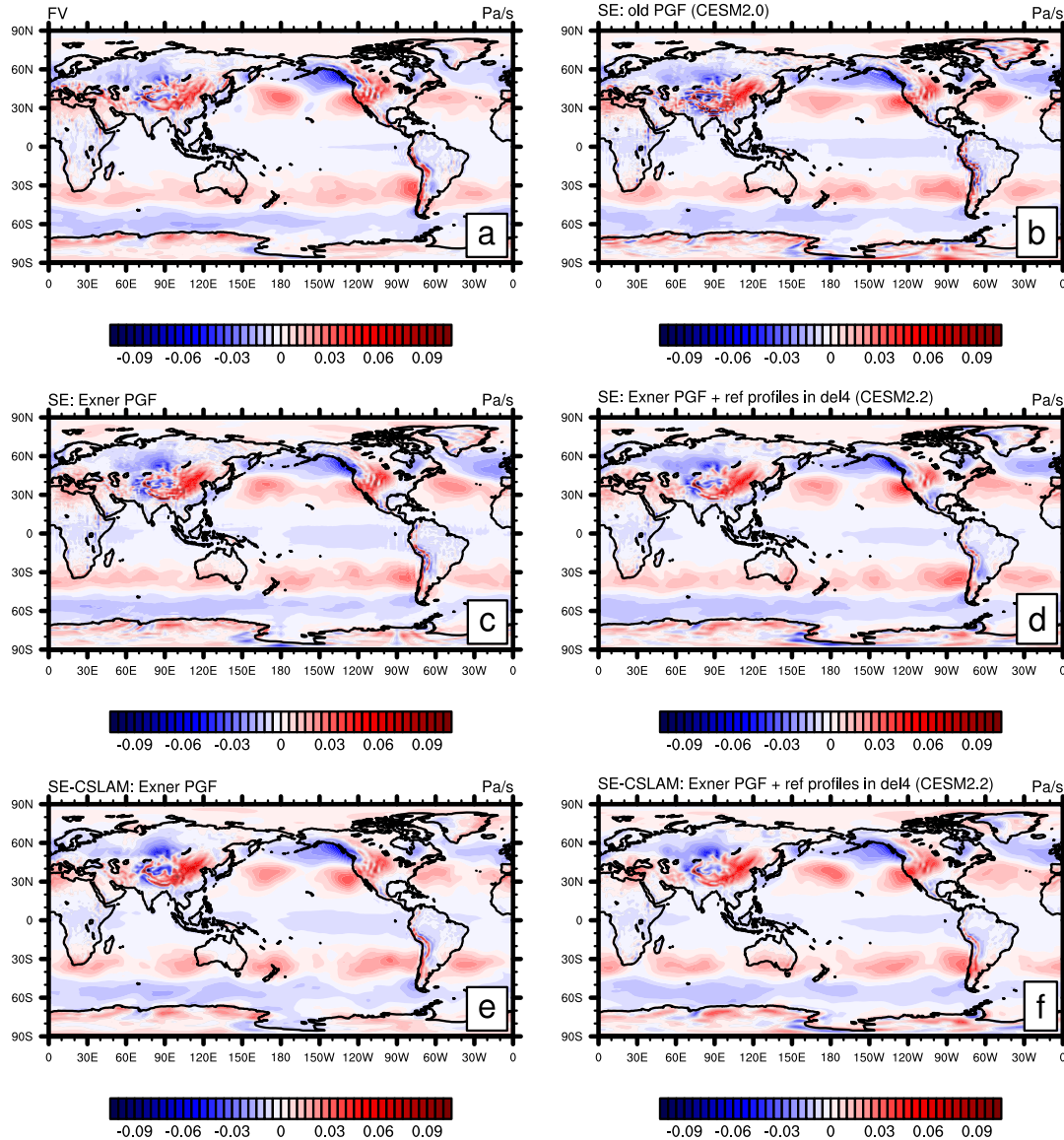


**Figure A2.** Same as Figure A1 but using modified Held-Suarez forcing and the average is over 18 months (excl. spin-up).